

Mosaic representations of odors in the input and output layers of the mouse olfactory bulb

Honggoo Chae^{1,4}, Daniel R. Kepple^{1,2,4}, Walter G. Bast¹, Venkatesh N. Murthy³,
Alexei A. Koulakov^{1,2*} and Dinu F. Albeanu^{1,2*}

The elementary stimulus features encoded by the olfactory system remain poorly understood. We examined the relationship between 1,666 physical-chemical descriptors of odors and the activity of olfactory bulb inputs and outputs in awake mice. Glomerular and mitral and tufted cell responses were sparse and locally heterogeneous, with only a weak dependence of their positions on physical-chemical properties. Odor features represented by ensembles of mitral and tufted cells were overlapping but distinct from those represented in glomeruli, which is consistent with an extensive interplay between feedforward and feedback inputs to the bulb. This reformatting was well described as a rotation in odor space. The physical-chemical descriptors accounted for a small fraction in response variance, and the similarity of odors in the physical-chemical space was a poor predictor of similarity in neuronal representations. Our results suggest that commonly used physical-chemical properties are not systematically represented in bulbar activity and encourage further searches for better descriptors of odor space.

Insight into the computations performed by sensory systems arises from understanding the stimulus features encoded by them, such as the wavelength of light and the frequency of sound¹. Unlike other sensory modalities (that is, vision and audition), it is not understood what properties of odors are important in olfaction, and how they are processed by the olfactory system. The relationship between odor structure (chemical space), the spatial and temporal patterns of activity in the brain (neuronal space) and the perceived odor quality (perceptual space) has been elusive^{2–9}. As a result, currently, one cannot robustly predict neuronal activity patterns and perceptual attributes starting from the physical features of odor molecules.

Even the earliest step in olfaction, the interaction between a particular odorant receptor (OR) and ligands (odorants) has defied simple descriptions. Since the olfactory system derives percepts on the basis of responses of a large number of OR types, the number of dimensions of the odor space could be large. Nonetheless, recent studies using dimensionality reduction methods have suggested that a relatively small number of odor physical-chemical descriptors (~30 out of ~1,600 to ~5,000 in the Dragon database¹⁰) capture odor similarity in all three spaces (chemical, neuronal and perceptual)^{5,11–15}. It has been proposed that most variance in human perceptual space can be explained by considering low dimensional manifolds (~2–20), with dimensions related to behaviorally relevant features such as stimulus pleasantness, toxicity and/or hydrophobicity^{2,5,7,12,16}.

The spatial layout and wiring patterns of neural circuits can offer important clues about the underlying computations; for example, a retinotopic organization along with nearest neighbor interactions enabled the inference of local contrast enhancement in the retina¹⁷. In the vertebrate olfactory system, there is a reproducible and precise layout of OR identity in the glomerular layer of the olfactory bulb (OB)¹⁸. However, how this receptor-based layout translates to a functional map remains unclear^{13,19–25}.

Odor information arriving at glomeruli from the olfactory sensory epithelium is modified within the OB by local and top-down interactions. Two classes of output neurons, mitral and tufted cells

(MTCs), convey information to several olfactory cortical and sub-cortical areas. These two output channels differ in their inputs, morphology, intrinsic excitability, local connectivity, activity patterns, downstream targets and top-down feedback^{26–30}.

Inspired by progress in the characterization of odors through the use of a large number of physical-chemical properties, here we investigate whether these features are represented in the neuronal activity patterns in the input and output layers of the bulb. We studied how the activity patterns of glomeruli and MTCs in awake, head-fixed mice relate to a set of commonly used 1,666 physical-chemical odor properties. We asked four questions. First, how well are these physical-chemical properties of odors captured by the glomerular and MTC responses? Second, does similarity of odor molecules in the physical-chemical properties space correlate with the similarity of neuronal population responses? Third, does the physical location of individual glomeruli or MTCs depend on their physical-chemical receptive fields? Finally, what is the relationship between neuronal odor representations in the input and output layers of the bulb?

Results

We used imaging of intrinsic signals from the dorsal surface of the OB to probe the responses of glomeruli ($n = 5$ mice, 10 bulb hemispheres (fields of view, FOVs), 871 glomeruli) to an array of chemically diverse odors (Supplementary Fig. 1; Supplementary Table 1; Methods). Previous reports have indicated that glomerular intrinsic signals approximate well the activity of presynaptic olfactory sensory neuron (OSN) terminals in the OB¹⁹. In separate experiments, we employed multiphoton microscopy to monitor the responses of MTCs (via GCaMP3/6, Methods) tiling the dorsal aspect of the bulb ($n = 8$ mice, 13 hemispheres, 19 FOVs, 1,711 mitral and tufted somata; Supplementary Figs. 1–3) to the same stimuli across a range of concentrations in awake mice (Methods).

Odor responses of glomeruli and MTCs are poorly described by Dragon physical-chemical properties. Previous studies have

¹Cold Spring Harbor Laboratory, Cold Spring Harbor, NY, USA. ²Watson School for Biological Sciences, Cold Spring Harbor Laboratory, Cold Spring Harbor, NY, USA. ³Department of Molecular and Cellular Biology and Center for Brain Science, Harvard University, Cambridge, MA, USA. ⁴These authors contributed equally: Honggoo Chae, Daniel R. Kepple. *e-mail: koulakov@cshl.edu; albeanu@cshl.edu

suggested that the olfactory system is tuned to extract specific physical–chemical features of odors^{11,12,31,32}. Here we investigated whether a wide array of physical–chemical molecular parameters are good predictors of glomerular and MTC responses. We used the Dragon database¹⁰ to evaluate 1,666 physical–chemical properties to each odor in the panel. The responsiveness of each glomerular or MTC region of interest (ROI) to a particular property (called here the property response) was characterized as a Pearson's correlation between the odor responses of the ROI and the values taken by the property (termed property strength vector (PSV)) across the 49 monomolecular odors used (Fig. 1a–c; Methods). The array of such correlations across the Dragon molecular properties is defined as the property response spectrum of that ROI (Fig. 1d,g). This definition is analogous to calculating a neuronal receptive field in the visual or auditory systems, whereby the response strength of a given cell is correlated with certain stimulus features. The property response spectrum represents the strength of individual ROI responses to an array of physical–chemical properties, thus playing the role of a molecular receptive field.

For both glomeruli and MTCs, the number of properties that single units responded to significantly (false discovery rate (FDR) of $q < 0.1$ for the property response spectrum of each ROI considered; Methods) varied from ROI to ROI, with an average of 12.7 per glomerulus and 16.4 properties per MTC (Fig. 1f,i). In general, individual responsive glomeruli and MTCs were only poorly tuned to the physical–chemical properties (Supplementary Fig. 4a,c; ~26% of glomeruli and ~33% of MTCs showed no significant correlations), and the vast majority of glomerular and cell odor response–property correlation pairs was not significant (Fig. 1d–i; Methods). Within the subset of significant glomerular and cell odor response–property pairs (~6%), correlations spanned both negative and positive values (absolute average: 0.35 ± 0.07 s.d. for glomeruli and 0.36 ± 0.08 s.d. for MTCs; Supplementary Fig. 4e). Across different experiments, the tuning widths (the number of significant properties per ROI) were similar (Supplementary Fig. 4b,d).

We further used principal component analysis (PCA) to quantify the dimensionality of three data types that describe the physical and neuronal odor representations (Fig. 1j–l). Approximately 17 dimensions (17D) were sufficient to account for 90% of the variance in the values taken by Dragon molecular properties (PSV) across the 49 odors used (Fig. 1l). Thus, many of these properties are redundant^{15,16}, and a 17D flat surface contains substantial amount of information (90%) on the molecular properties. The dimensionality of the physical–chemical descriptors depends on the odors included in the panel, and, in principle, can be independent of the responses of olfactory neurons. In comparison, the responses of glomeruli to odors in our panel could be described within a 21D principal component (PC) space, and those of the MTCs in a 24D space at the same level of variance explained (90%; Fig. 1j,k). We iteratively sampled increasing number of odors (up to 49; Methods) and observed that the dimensionality of the molecular properties and the glomerular and MTC responses steadily increased. Thus, the quantities reported here represent lower bounds on these metrics of odor space. MTC responses generally exhibited higher dimensionality than glomerular responses, which is consistent with previous reports of a decorrelation of glomerular inputs within the bulb^{20,33–36} (Supplementary Fig. 4f,g).

Do neuronal responses efficiently represent Dragon molecular properties? We used a computational technique, which we call principal component exchange (PCX), and projected the molecular properties (PSV) into the PC space of neuronal responses (glomerular or mitral; Methods). We then computed the variance of the molecular properties data captured by the neuronal responses PC space of increasing dimensionality (Fig. 1j,k). If the PC spaces of the molecular and neuronal responses were identical, then glomerular (or mitral cell) PCs would capture the same fraction of

variance in both of the datasets for neuronal responses and molecular properties. Instead, we found that the PCs of glomerular and mitral cell responses explain almost the same fraction of variance in the molecular properties dataset as they do in randomly generated data (Methods; gray and black lines, Fig. 1j,k). When projected to the PC space of molecular properties, glomerular and mitral cell responses were also similar to random data controls in terms of the amount of variance explained (Fig. 1l; same for tufted cells, data not shown). To better characterize the performance of PCX, we used surrogate data in which a known relationship was embedded. We systematically perturbed the glomerular odor response vectors by adding known amounts of noise as a variable. As expected, the gradual injection of noise resulted in less and less variance explained by the glomerular PCs. Corrupting the glomerular responses signal-to-noise ratio (SNR) by more than fivefold led to similar amounts of variance explained as by the molecular properties (Supplementary Fig. 4h). Projecting mitral cell responses in the glomerular PC space, or glomerular responses in the mitral cells PC space, captured less variance compared with the reference PC spaces (glomerular and mitral), but substantially more than random data, as discussed later (Supplementary Fig. 4h). Recording glomerular responses in anesthetized mice, or sampling MTC responses within shorter intervals (0.5 s to 1.5 s) from stimulus onset, led to similar results (Supplementary Fig. 5).

Overall, our data show that neural responses of both glomeruli and OB outputs are poorly tuned to the analyzed physical–chemical properties, and instead reflect odor features that are not captured well by these molecular properties, which are commonly used in computational chemistry, and by previous studies of olfaction.

Odor similarity in the physical odor space is a poor predictor of neuronal representations.

Does the similarity between pairs of odors, calculated using the set of 1,666 physical–chemical properties, reflect the similarity in neuronal representations of the same odors in either the input or output layers of the OB? To describe the similarity in odor physical space for each odor pair in the panel, we calculated the Euclidean distance between the normalized molecular property strengths associated with each odor in the panel as proposed by previous studies^{11–13,37}. To represent odor similarity in the neuronal representations, we used the following two metrics: the Euclidean distance between the ROI responses to the same pair of odors and the Pearson's correlation in neuronal responses (pooling data across FOVs, Methods). For both glomeruli and MTCs, the pairwise odor similarity in the space defined by the physical–chemical properties had only poor and variable correlation with the similarity in neuronal representations (Fig. 2a,b).

It may be that only a small subset of molecular properties has a robust relation to the neural responses. To address this question, for each odor pair, we built a sparse regression between the squared pairwise odor response distances and the squared differences between individual physical–chemical property values. We used a non-negative least absolute shrinkage and selection operator (LASSO) algorithm that selects a sparse subset of non-zero properties from the full set to better explain the differences in neuronal responses³⁸ (Methods). The properties were selected to yield the best fit of pairwise distances in neuronal responses and physical–chemical space by weighting the odor similarity calculated in the physical–chemical space. Using this approach, we identified small subsets of properties that are reflected well in the neuronal responses. For example, using ten molecular properties selected via LASSO, the correlation between the pairwise odor distances in physical–chemical and neuronal responses increased substantially (~0.60; we ran the LASSO algorithm independently for the glomerular and MTC datasets, Methods). The inclusion of more properties into the analysis mildly improved the correlation (40 properties increased the correlation score to ~0.65; Fig. 2c,d).

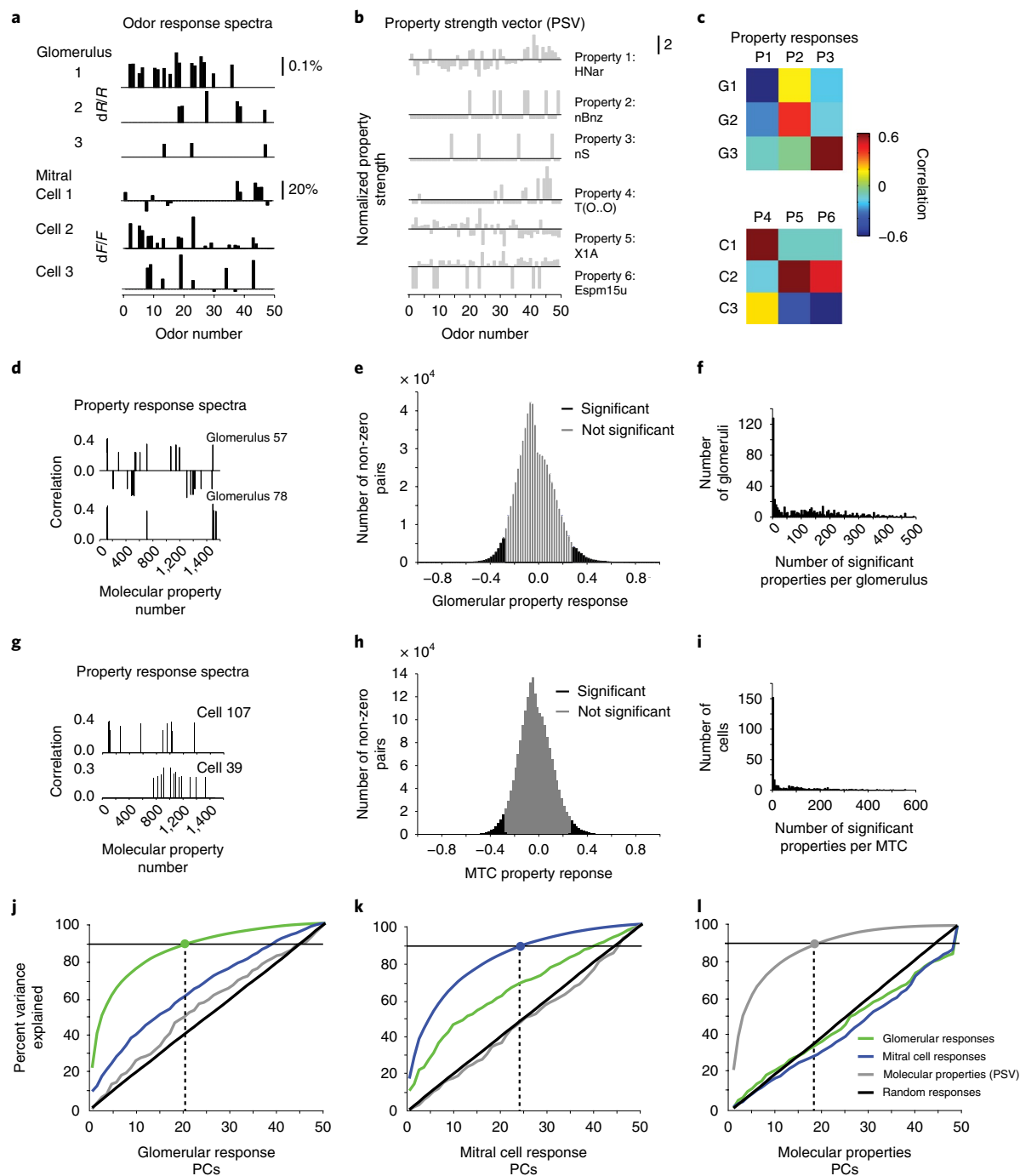


Fig. 1 | Tuning of glomeruli and MTC responses to Dragon physical-chemical properties. **a**, Odor responses of three example glomeruli and mitral cells. The responses ($-dR/R$, dF/F) are shown for a panel of 49 monomolecular odors. Nonsignificant responses were set to zero (Methods). **b**, Six example molecular PSVs across the same odors as used in **a**. HNar, Narumi harmonic topological index; nBz, number of benzene rings; nS, number of sulfur atoms; T(O..O), sum of topological distances between oxygen atoms; X1A, average connectivity index of order 1; Espm15u, spectral moment of order 15 from edge adjacency matrix. **c**, Property responses given by the Pearson's correlation coefficients between the odor responses (**a**) of the three example glomeruli (upper) and mitral cells (lower), and the six example molecular PSVs (**b**) calculated over 49 odors in the panel. **d,g**, Example correlations (property response spectra) between odor responses and molecular properties for two example glomeruli (**d**) and mitral cells (**g**). **e,h**, Distribution of the glomerular response-molecular property (**e**; $n = 13,446$) and MTC response-molecular property (**h**; $n = 27,992$) pairwise Pearson's correlations (two-sided t -test, $P < 0.05$, FDR $q < 0.1$; Methods). **f,i**, Histogram of the number of molecular properties that individual glomeruli (**f**; $n = 13,446$) and MTCs (**i**; $n = 27,992$) respond to, above the significance threshold (two-sided t -test, $P < 0.05$, FDR $q < 0.1$; Methods), with an average of 12.7 per glomerulus and 16.4 per MTC. **j-l**, Results of PCA for glomerular (**j**; $n = 871$ glomeruli), mitral cell responses (**k**; $n = 639$ mitral cells) and molecular properties (**l**; $n = 1,320$ properties). The percent of variance explained is shown as a function of the number of included PCs. **j**, The percent variance explained of glomerular and mitral cell odor responses, molecular PSVs and random data controls shown as a function of included PCs of glomerular responses. **k,l**, The percent variance explained of glomerular and mitral cell odor responses, molecular PSVs and random data controls shown as a function of the number of included PCs of mitral cell responses (**k**) and of molecular properties (**l**).

We further determined how these regression analyses and correlations generalize across different FOVs (FOV cross-validation) and odor pairs (odor cross-validation, Methods). Cross-validation across FOVs only slightly decreased the observed glomerular responses to physical space correlations, which is consistent with reproducible glomerular odor maps across individuals¹⁹. The same procedure, however, resulted in substantially lower correlations (~ 0.2) for the MTC responses, which may reflect differences in sampling MTCs along the dorsal aspect of the OB across FOVs. In contrast, the odor cross-validation procedure, or the combination of these two procedures, drastically diminished the correlations to the physical–chemical representations (at most ~ 0.10 for glomeruli and ~ 0.05 for MTCs; Fig. 2c,d, Methods). Employing a greedy algorithm (Methods) with odor cross-validation for the MTC data led to qualitatively similar results (Supplementary Fig. 4j).

For the glomerular data from awake and anesthetized mice and the MTC response data in awake mice, we also performed the LASSO analysis on shuffled controls, whereby the Dragon properties were shuffled by odor identity while keeping the neuronal responses unchanged (Fig. 2e,f; Supplementary Fig. 5e). Interestingly, searching for sparse subsets of shuffled properties with regularization increased the correlation between pairwise odor similarity in the physical and neuronal spaces (for both glomerular and MTC responses). A drastic decrease in correlation occurred after performing cross-validation across odors and FOVs (Fig. 2e,f; Supplementary Fig. 5e).

Thus, while correlations between similarity in physical–chemical and neuronal response spaces could be identified using subsets of molecular properties, they held little predictive power when new odor pairs or shuffled properties were tested, suggesting that such correlations emerge due to overfitting.

Relating the tuning of glomeruli and MTCs to molecular properties to their placement on the bulb. Previous experiments in the glomerular layer of the rodent OB have provided contrasting views of spatial organization. Some authors have suggested that different classes of chemicals are represented in a spatially segregated manner, perhaps even in an ordered topographic manner^{25,39–41}. Others have noted a great deal of local disorder, with no evidence of a smoothly varying representation^{13,19,42}. To date, these spatial relations have not been assessed using physical–chemical properties of odors, such as those provided by Dragon. Although our above-described analysis

has shown that glomeruli and MTCs sample a small subspace of the properties (Fig. 1), some of these parameters are represented in the neuronal responses. Therefore, we investigated whether tuning to the molecular properties is spatially laid out in a systematic fashion at the level of glomeruli and MTCs.

For each property, we characterized the relationship between the tuning of glomerular and MTC responses and the spatial location of glomeruli and cells along the anterior–posterior (AP) and medial–lateral (ML) axes of the bulb. The tuning of individual glomeruli or MTCs was described by their property responses. For the ensemble of ROIs monitored in each FOV, we computed the correlation between the location for each ROI and its response sensitivity to each property, using FDR correction to account for false positives given the large number of properties. For each FOV (2D plane), every molecular property was described by the strength of its correlation along the AP and ML axes (Figs. 3a–f and 4a,b; Methods).

To determine whether any specific directions on the bulb surface are well aligned with independent combinations of the molecular properties, we performed PCA on the glomerular data to identify new relevant orthogonal reference axes (PC1 and PC2; Fig. 3a, Methods). Across different animals, the first principal axis (PC1; Fig. 3, blue) was consistently rotated approximately 40° (average = 38.7 ± 16.3 s.d.) with respect to the AP direction. Several molecular properties (20) appeared correlated (positively and negatively, FDR of $q < 0.1$) with PC1 (Fig. 3c,e; Supplementary Table 2), and could be robustly identified across animals (11 out of 12 hemibulbs). The properties correlated with the PC2 axis were much less consistent across samples (2 out of 12 hemibulbs; Fig. 3d,f). Two independent imaging sessions were included for one of the five mice.

The responses of glomeruli are predictive of their location on the bulb surface at a coarse spatial scale. Could the positions of individual glomeruli on the bulb be inferred using the properties they are responsive to? We tested this hypothesis by building a sparse linear regression for individual glomerular positions based on their tuning (property response spectra) to the molecular properties. Regression was obtained as described above, using the LASSO algorithm and selecting a small subset of active properties (20) from the full set (Methods). To quantify the quality of prediction, we evaluated the prediction error for each glomerulus for PC1 and PC2 normalized by the average glomerulus size (AGS)¹⁹. We found that glomerular positions are defined more

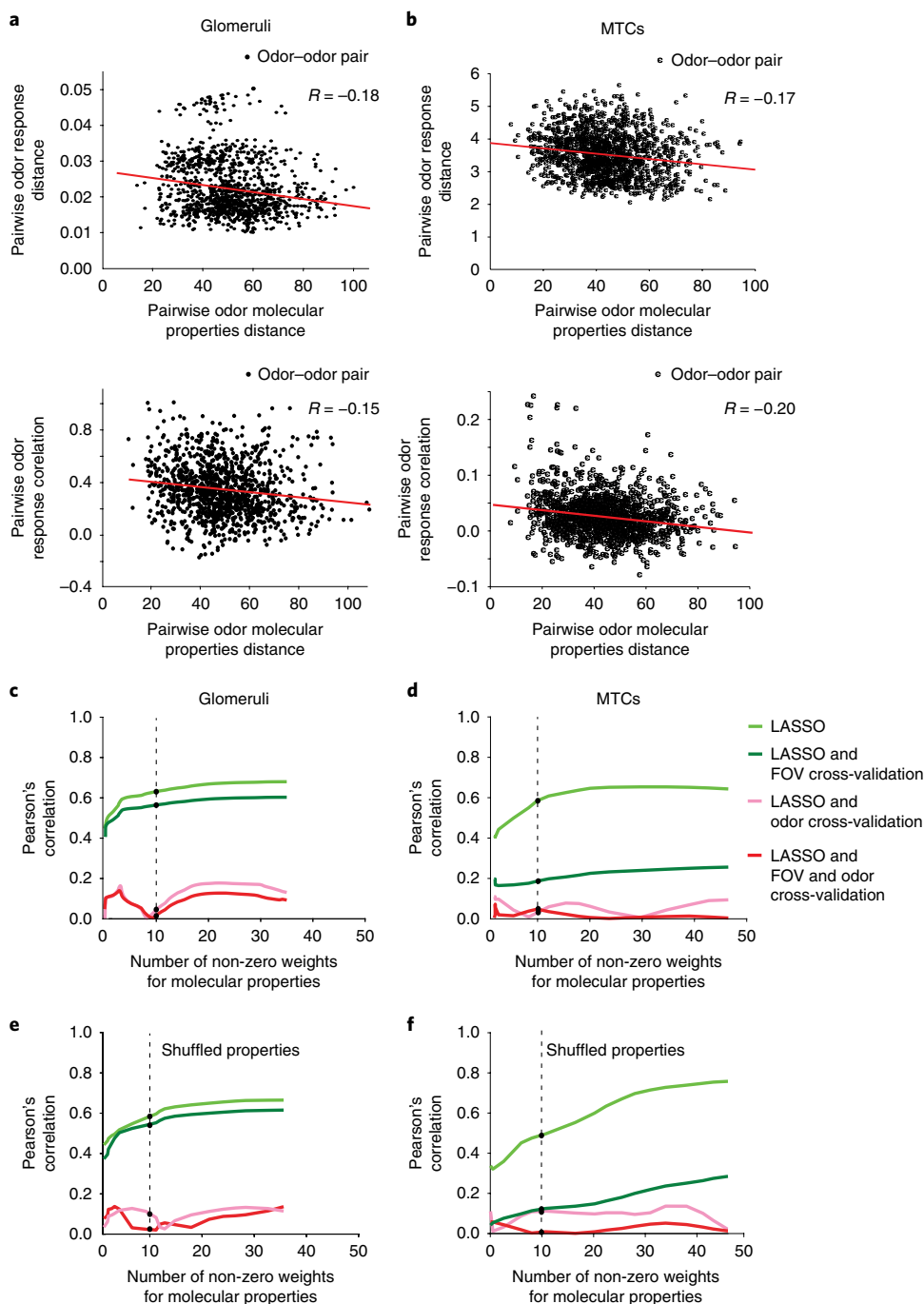
Fig. 2 | Pairwise odor similarity comparison across physical–chemical and neuronal response odor representations. **a**, Pairwise odor Euclidean distance across Dragon physical–chemical properties versus distance between glomerular responses, expressed as the Euclidean distance ($n = 1,176$ odors pairs, upper) and Pearson's correlation ($n = 1,176$ odors pairs, lower). **b**, Pairwise odor Euclidean distance across Dragon physical–chemical properties versus distance between MTC responses, expressed as the Euclidean distance ($n = 1,176$ odors pairs, upper) and Pearson's correlation ($n = 1,176$ odors pairs, lower). Note that the average odor response Euclidean distances for glomeruli and MTC representations are expected to differ since they are determined by the absolute strength of intrinsic and fluorescence signals. **c**, LASSO regression based on a subset of physical–chemical properties selected from the 1,666 set describing the relationship between odor pairwise similarity across properties versus glomerular responses. The light green line indicates that all the imaged hemibulbs were used as a training set for optimizing the regression. The dark green line indicates that half of the FOVs were used as a training set and the remaining half for cross-validation (FOV cross-validation). The pink line indicates that all imaged hemibulbs were used for training, while one pair of odors was iteratively left out during training and added back subsequently for cross-validation (jackknife, odor cross-validation). The red line indicates that half of the FOVs were used for training and the remaining half for cross-validation; in addition, one pair of odors was iteratively left out during training and subsequently added back for cross-validation (jackknife, FOV and odor cross-validation). **d**, LASSO regression based on a subset of physical–chemical properties selected from the 1,666 set describing the relationship between odor pairwise similarity across properties versus MTC responses. The light green line indicates that all FOVs of imaged MTCs were used as a training set for optimizing the regression ($R = 0.68$). The dark green line indicates that half of the FOVs were used as a training set and the remaining half for cross-validation (FOV cross-validation, $R = 0.2$). The pink line indicates that all imaged FOVs of MTCs were used for training, while one pair of odors was iteratively left out during training and added back subsequently for cross-validation (jackknife, odor cross-validation, $R = -0.06$). The red line indicates that half of the FOVs were used for training and the remaining half for cross-validation; in addition, one pair of odors was iteratively left out during training and subsequently added back for cross-validation (jackknife, FOV and odor cross-validation, $R = -0.08$). The broken line corresponds to an instantiation of the LASSO regression, when only ten physical–chemical properties were allowed to take non-zero weights. **e,f**, LASSO was implemented to describe the relationship between odor pairwise similarity across properties and glomerular (**e**) or mitral cell (**f**) responses using shuffled molecular properties; the PSV associated with a given odorant was randomly swapped with the PSV of another molecule in the panel without manipulating the neuronal responses (the colors of the lines are as for **d**).

precisely along the PC1 versus PC2 axis (s.d. = 3.8 versus 4.7 AGS; Fig. 3g,h). Importantly, shuffled controls (obtained by randomizing the identity of molecular properties, while not altering the glomerular responses) produced statistically indistinguishable outcomes in the prediction of glomerular positions by using shuffled property responses along newly computed PC1 and PC2 axes (Fig. 3g,h). We also performed the same regression analysis using only the odor response spectra of individual glomeruli and reached quantitatively similar results (Fig. 3g,h).

Overall, these results indicate that responses of glomeruli to odors are predictive of their coarse placement on the bulb surface, which is consistent with previous reports relating the odor spectra and location of glomeruli^{19,25,41}. Our results also suggest that the correlations observed between the topography of glomerular odor

representations and the physical–chemical properties cannot be distinguished from effects of overfitting (chance level) due to the large number of Dragon properties.

Tuning of MTCs to molecular properties is not correlated with their spatial location. We further investigated the relationship between the location of OB output neurons and their tuning to molecular properties. In general, MTC responses in a FOV were locally heterogeneous, responding to chemically diverse odors (Supplementary Fig. 6). Most sampled FOVs showed very few or no significant correlations at all (Fig. 4a,b). Strikingly, in one FOV (no. 21, tufted cells), several properties were correlated with both AP and ML axes of the bulb. Given previous results⁴³, and the relatively small size of individual FOVs sampled (~300–500 μm), we hypothesized



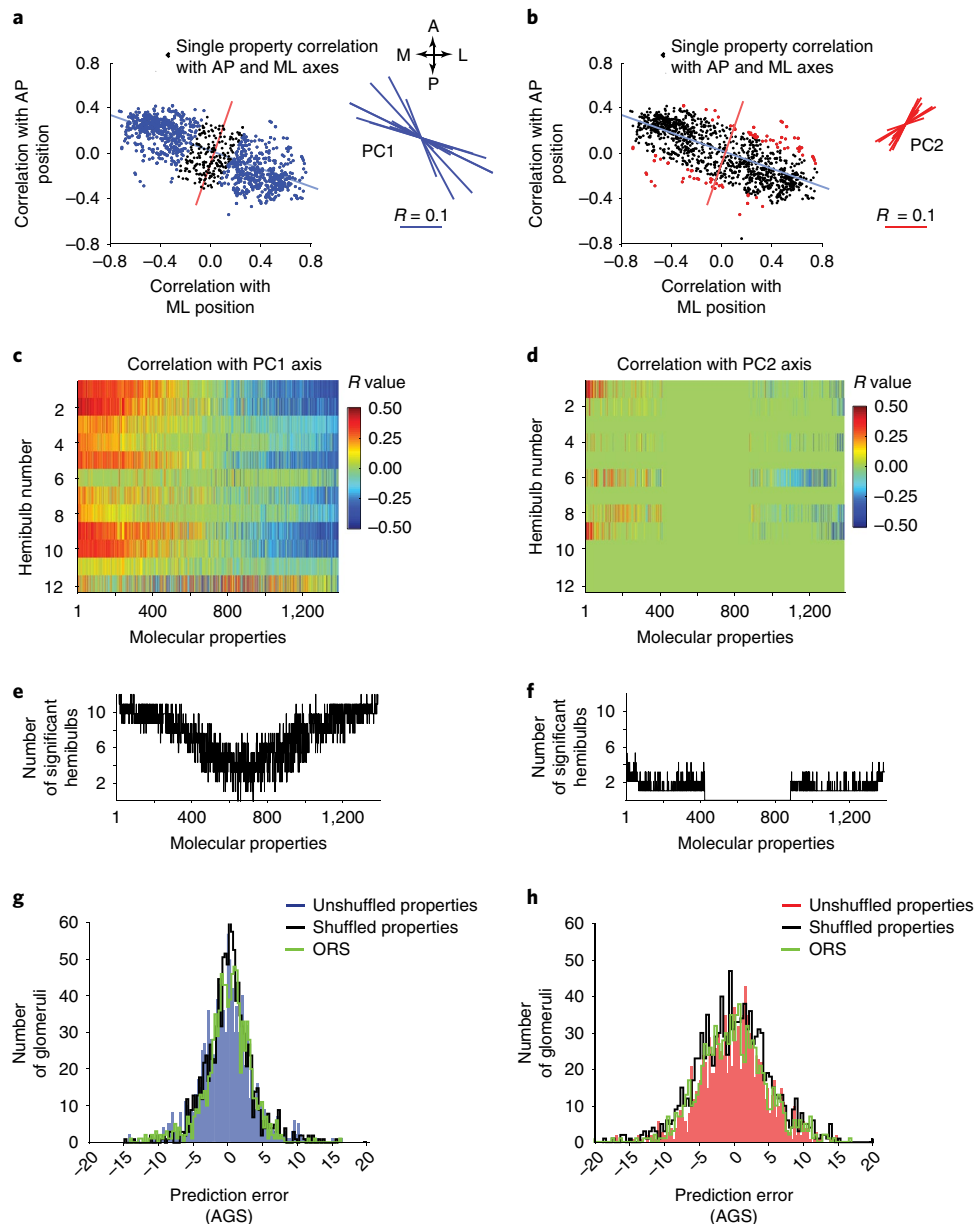


Fig. 3 | Weak spatial correlations between glomerular positions and molecular property responses. **a, b**, Pearson's correlations between individual property responses ($n=1,320$ properties) and the placement of glomeruli along the AP and ML axes of the bulb. Each circle represents the Pearson's correlation value of an individual molecular property. Performing PCA on the cloud of molecular property correlations computes the orientation of the first PC (PC1, blue) with respect to the AP and ML anatomical axes. Properties shown by blue and black circles correspond to significant and nonsignificant correlations, respectively, with the PC1 axis (two-sided t -test, $P < 0.05$, FDR $q < 0.1$). Red circles show properties significantly correlated with the PC2 axis (orthogonal on PC1, two-sided t -test, $P < 0.05$, FDR $q < 0.1$). Orientations of the PC1 and PC2 axes in 12 hemibulbs (bulb hemispheres) are shown by blue and red lines. **c, d**, Pearson's correlations between individual molecular properties and glomerular positions along the PC1 and PC2 axes for each hemibulb. In each panel, properties are re-sorted with respect to the strengths of correlation. For the panel of odors used, several properties (~ 300) did not take non-zero values, and were not included in the analysis. **e, f**, Number of hemibulbs in which a given molecular property is significantly correlated with the glomerular position along PC1 (**e**) and PC2 (**f**) (two-sided t -test, $P < 0.05$, FDR $q < 0.1$). A set of properties was consistently correlated with the PC1 axis (at most 11 out of 12 hemibulbs). Correlations along the PC2 axis were less consistent across samples (at most 2 out of 12 hemibulbs). **g, h**, Histograms of normalized displacement error vectors between the location of observed and predicted glomerular locations along PC1 (blue) and PC2 (red) axes. The predictor was obtained using a LASSO algorithm (jackknife cross-validation) to build a sparse linear regression based on 20 molecular properties (Methods). The prediction error is shown along PC1 (left, s.d. = 3.8 average glomerular size, AGS) and PC2 axes (right, s.d. = 4.7 AGS). Black traces correspond to prediction errors obtained for shuffled molecular properties control analyses; in this control, the PSV associated with a given odorant was randomly swapped with the PSV of another molecule in the panel without manipulating the neuronal responses. Green traces correspond to prediction errors obtained by running the regression analysis on the glomerular odor response spectra (ORS).

that such correlations could arise because of the similarity in the responses of groups of sister cells receiving inputs from the same glomerulus. If, for example, two of such sister cell groups are on

opposite sides of a FOV, we may observe a correlation between the locations of cells and tuning arising from differences in the responses of these sister cell groups.

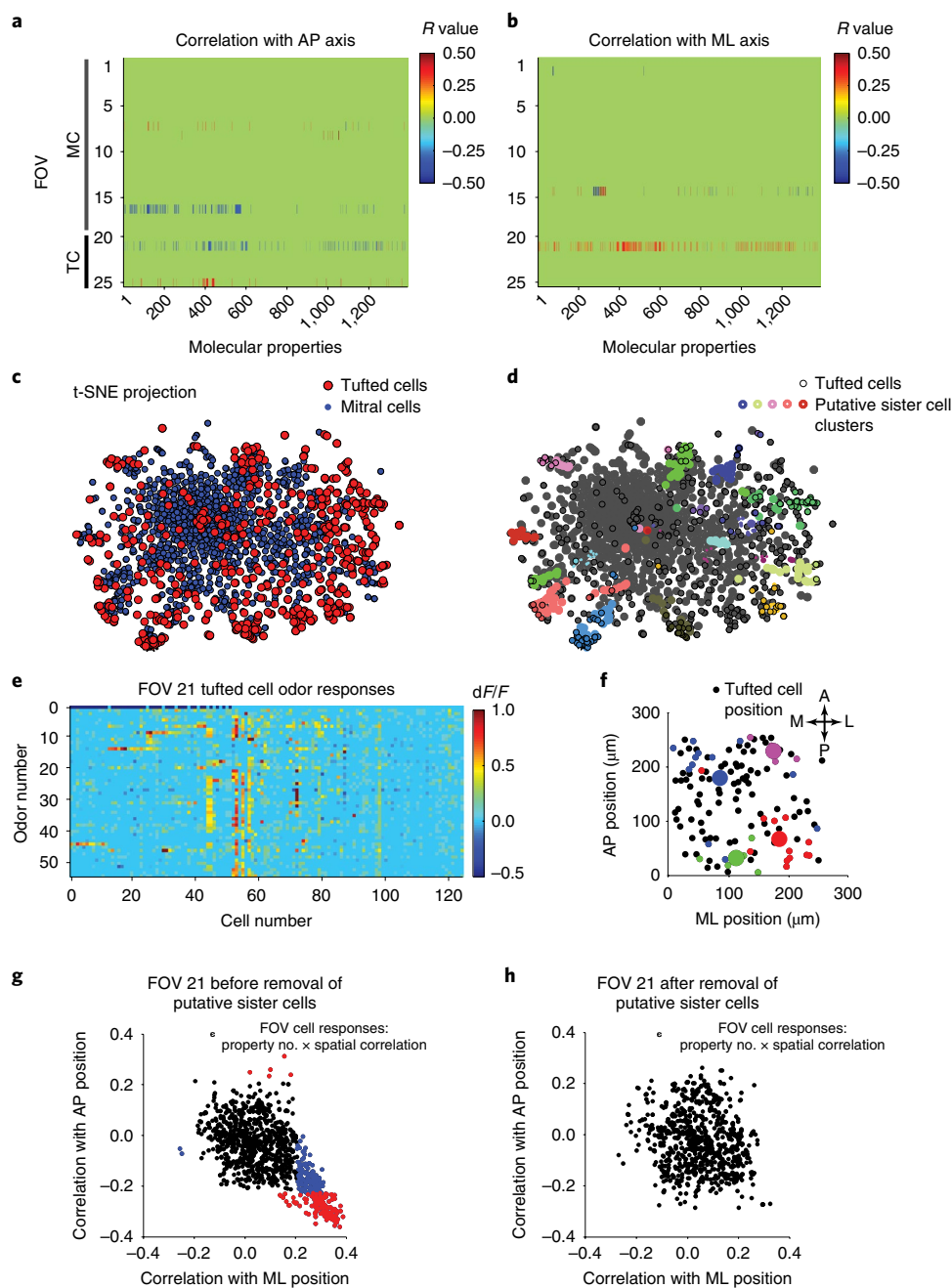


Fig. 4 | Lack of correlation between MTC placement and physical-chemical odor properties. **a,b**, Pearson's correlation coefficients between MTC locations with respect to the AP (left) and ML (right) axes within FOVs (rows) and their response sensitivity to individual properties across the physical-chemical properties analyzed. Only significant correlations are shown (two-sided *t*-test, $P < 0.05$, FDR $q < 0.1$). FOVs were sorted for MTCs for both nominal dilutions (1:100 and 1:3,000, 19 FOVs, 6 imaged for both dilutions). **c**, t-SNE projection of responses of all sampled MTCs. Each circle represents an individual MTC from 1 of the 19 FOVs imaged (1,205 mitral cells and 506 tufted cells). **d**, Same t-SNE projection as in **c** with different putative co-glomerular clusters ($n = 15$) shown by different colors. Tufted cell responses are represented by black circles. **e**, Odor responses (dF/F) of tufted cells from the example FOV (no. 21) sorted by size of functional clusters (Methods). Horizontal bars (upper) mark clusters of putative co-glomerular sister cells. **f**, Positions of tufted cells in the example FOV. Color circles mark clusters of putative sister cells. Larger colored circles correspond to the average location of putative sister cells within a given functionally defined cluster. **g,h**, Example FOV illustrating the correlation of physical-chemical properties with the placement of cells along the AP and ML axes of the bulb before (**g**) and after (**h**) removal of putative co-glomerular sister cells via odor-tuning-based clustering. Each point represents an individual molecular property ($n = 1,320$). Properties significantly correlated (two-sided *t*-test, $P < 0.05$, FDR $q < 0.1$) with either AP or ML axes are displayed as blue ($n = 160$) and red ($n = 288$) circles, respectively; black circles represent nonsignificant correlations.

To identify putative sister cells, we clustered cells based on the similarity in their responses to odors (Methods; Supplementary Fig. 6). Clustering was performed within and across FOVs, since sister MTCs receiving primary input from the same glomeruli are

expected to be found on the dorsal aspect of the bulb in multiple animals. The results of clustering are displayed using a T-distributed stochastic neighbor embedding (t-SNE) projection⁴⁴ in Fig. 4c,d. After clustering, we collapsed the major clusters of cells into single

'average' cells, with both responses to odors and positions represented by the average value within each cluster (Fig. 4e,f). When this approach was used, all significant correlations between tuning to molecular properties and the locations of cells vanished (Fig. 4h).

MTCs and glomeruli sample different molecular subspaces. We found that glomerular and MTC odor responses differ in their overall dimensionality, capture different amounts of variance with respect to tuning to the Dragon molecular properties and display varying degrees of spatial correlation to these descriptors. We further investigated the differences in glomerular and MTCs in their sampling of the odor space.

First, using the PCX method, we compared the amount of variance in MTC and glomerular responses captured by the PCs of the glomerular responses to the 49 stimuli. If MTC and glomerular response spaces were similar, the glomerular PCs would explain nearly the same fraction of variance in both the mitral cell and glomerular datasets. However, glomerular PCs explained substantially less variance in the mitral versus glomerular responses (Fig. 5a). Similarly, the PCs calculated for mitral cell odor responses were insufficient to describe the glomerular responses. However, the mitral cell PCs performed well in capturing tufted cell responses (Fig. 5a).

One explanation for the differences in the PC spaces of glomerular and mitral cell responses is a sampling bias in probing the two layers, since our data include a small population of mitral cells and glomeruli, albeit from the same region of the bulb. In an attempt to reconcile the glomerular and mitral cell data, we tested a random selection model in which the responses of MTCs reflect the responses of individual glomeruli (Methods). Within this model, the discrepancy between the sampled spaces of glomerular and model mitral cells is small (Fig. 5b, green versus broken blue lines) and not compatible with the experimental data (Fig. 5a, green versus blue lines).

We sought to identify an alternative model that could better explain the relation between glomerular and mitral cell odor spaces. We computed a rotation matrix in the odor space, which could convert the glomerular PCs to the mitral PC space. More precisely, if \hat{R}_G is the matrix of glomerular responses (glomeruli \times odors), we generated surrogate mitral cell responses \tilde{R}_{MC} (mitral cells \times odors) using the following equation:

$$\tilde{R}_{MC} = \hat{R}_G \cdot \hat{Q} \quad (1)$$

Here \hat{Q} is the (odors \times odors) rotation matrix ($\hat{Q}^T \hat{Q} = \hat{I}$) that relates the glomerular and mitral cell odor spaces. To derive \hat{Q} , we used singular value decomposition. We call this transformation the rotation model, since, to produce model mitral cell responses, it mixes glomerular responses to different odors with coefficients provided by rotation matrices (Methods). We found that the responses of model mitral cells (generated from glomerular responses; Fig. 5c, broken blue lines) are close to the variance produced by actual mitral cell responses (Fig. 5c, blue unbroken lines), while those obtained from shuffled glomerular controls differ widely (Supplementary Fig. 7). Thus, a simple rotation (equation (1)) can generate mitral cell responses from glomerular responses and vice versa. The discrepancies between the rotation model and experimental data can be explained by the lower dimensionality PC space occupied by glomeruli (Fig. 1g,h). Thus, surrogate mitral cell responses (Fig. 5c, right) are left-shifted compared to the real cell responses because the dimensionality of the glomerular PC space is lower (21D versus 24D; Supplementary Fig. 4f,g). The rotation model reflects the possibility that MTCs sample a subset of the glomerular PCs, as well as other (top-down) stimulus-related information (that is, expectation or behavioral value), which are under-represented in the glomerular input^{27,30,45}.

Our model aims to relate the odor representations in the input and output layers of the OB. The model described by equation (1) uses a small number of parameters (odors \times odors) to mix glomerular responses to different odorants and yield MTC responses. An equivalent circuit-level model (Methods) pools together inputs from multiple glomeruli to produce MTC responses⁴⁶ using a substantially larger number of parameters.

To further characterize the differences between glomerular and MTC response odor subspaces, we employed a statistical method called canonical correlation analysis (CCA)⁴⁷. CCA identifies a set of angles (Jordan principal angles) that describe the relationship between two subspaces (that is, glomerular and mitral) embedded into the same multidimensional space. The cosine of the Jordan principal angle is the canonical correlation coefficient. For two 2D planes in 3D, for example, one of the Jordan angles is the angle between the planes. In spaces of higher dimension, the number of non-zero Jordan angles is larger than one (see Methods for a description of the number, distribution and relationship between Jordan angles and the degree of overlap between subspaces).

Calculating the distribution of Jordan principal angles between PC spaces of increasing dimensionality indicated that glomerular and mitral cell odor response spaces are distinct but related (Fig. 5d,e; Supplementary Fig. 8; Methods). The distribution of Jordan angles between mitral cells and glomerular PC spaces (Fig. 5d, blue line) was matched by a glomeruli versus glomeruli distribution when noise was added to one set of glomerular responses with a SNR of ~ 1.0 . This analysis suggests that mitral cells mix inputs from glomeruli and additional information from other sources in a roughly equal proportion.

Overall, we propose that the odor spaces of glomerular and mitral cell responses are related via a rotation transformation. This transformation mixes responses obtained for different odors with predictable real-value coefficients, and may reflect the interplay between local processing and top-down centrifugal inputs to the bulb.

Discussion

We sampled odor responses of OB inputs and outputs in awake, naive head-fixed mice, and sought to relate this activity to the physical-chemical properties of odors. Our experiments show that odors activate glomeruli and MTCs in a mosaic, spatially dispersed manner, with poor relation to an extensive set of commonly used physical-chemical molecular properties. Specifically, odors with similar physical-chemical descriptors did not elicit similar activity in the neuronal representations. Molecular properties were insufficient to explain the overall variance in neural odor responses, and lacked predictive power for the placement of both glomeruli and MTCs. Comparing activity patterns across the input and output layers, we found that glomeruli and MTCs sample different stimulus subspaces, and identified a rotation transformation in odor space that can relate these two sensory representations.

Dimensionality of the OB odor responses. The estimates of the dimensionality of odor space vary widely, ranging from several hundred, based on the number of odorant receptor types, to just two to ten based on human perceptual responses^{5,16}. This is different, for example, from our understanding of color vision. In the visual system, three types of cone receptors form the three dimensions on which any neuronal and perceptual visual representations can be built⁶. In our experiments, the responses of a set of glomeruli and MTCs from the dorsal aspect of the bulb to a panel of 49 stimuli could be well described within a ~ 20 D flat PC space (Fig. 1). This is a lower bound on the dimensionality of bulb neuronal representations, since systematically increasing the number of odors included in the analysis led to a steady increase in the dimensionality of responses (Supplementary Fig. 4f). However, this ~ 20 D PCA space

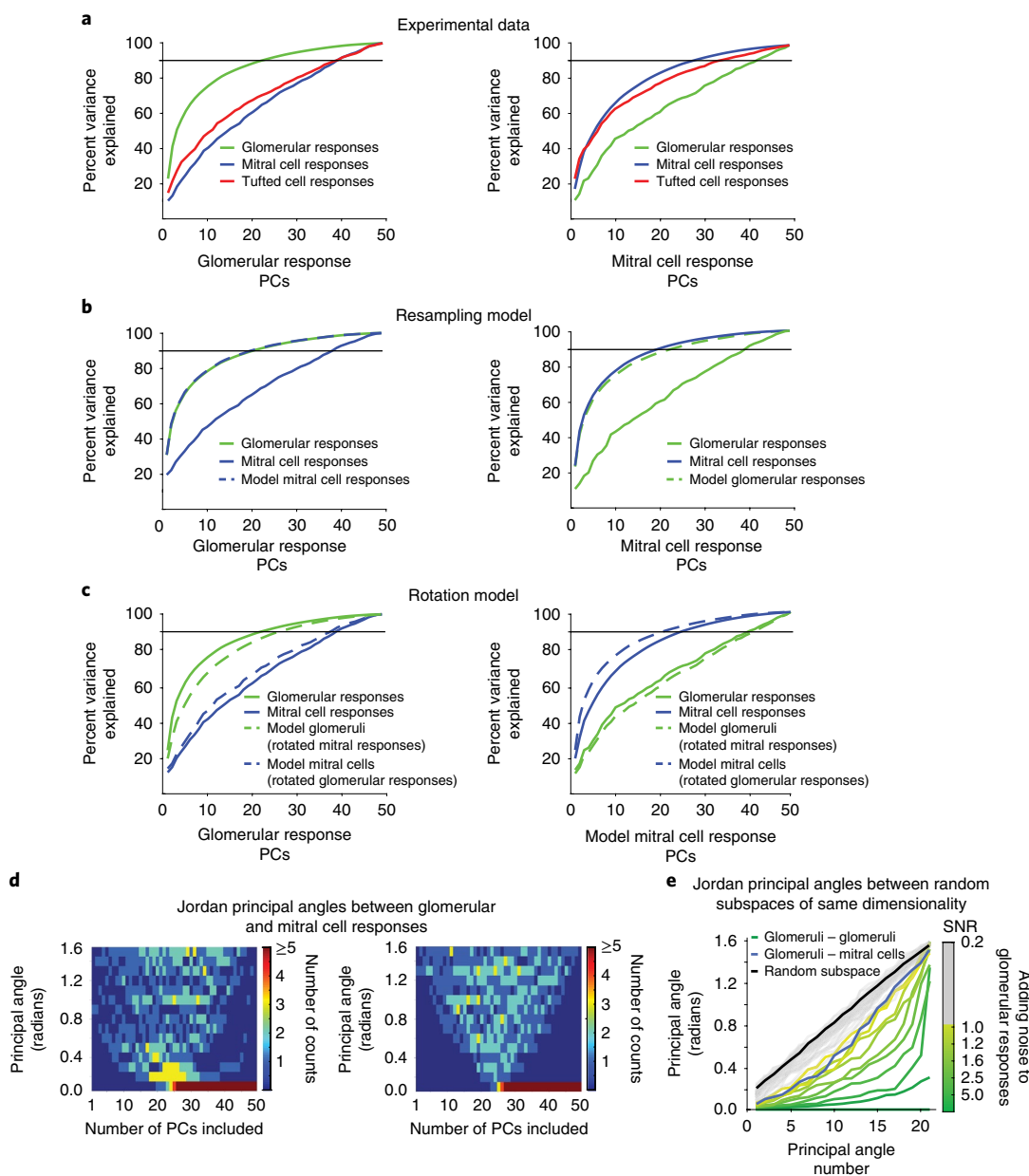


Fig. 5 | Comparison of glomerular and MTC odor response spaces. **a**, Left: the percent variance explained of glomerular and MTC responses shown as a function of the number of included glomerular PCs. Right: the percent variance explained of glomerular and MTC odor responses shown as a function of the number of included PCs of mitral cell responses. **b**, Re-sampling model to explain the discrepancy between glomerular and mitral cell odor spaces. Model mitral cell responses were generated by taking samples from the glomerular responses. Left: the percent variance explained of glomerular, mitral and simulated model mitral cell responses shown as a function of the number of included glomerular PCs. The simulated mitral cell response variance appears similar to the explained glomerular variance and deviates from experimentally observed mitral cell responses. Right: the percent variance explained of glomerular, mitral and simulated glomerular responses shown as a function of the number of included PCs of mitral cell responses. **c**, Model mitral cell responses were generated by rotating glomerular responses in odor space. Similarly, model glomerular responses were generated by rotating mitral cell responses. Left: the percent variance explained of glomerular, mitral cell, simulated model mitral cell and model glomerular responses shown as a function of the number of included glomerular PCs. Right: the percent variance explained of glomerular, mitral cell, simulated mitral cell and model glomerular responses shown as a function of the number of included PCs of model mitral cell responses. **d**, Jordan principal angles between the glomerular and mitral cell odor response subspaces (left) and random subspaces of the same dimensionality (right) as a function of number of PCs included in the analysis. PCs are sorted in descending order of explained variance. To maintain contrast in the color scheme rendering the number of counts in the 2D histogram, the 0 bin angle entry in the 2D histogram was re-scaled. **e**, Jordan principal angles (radians) between glomerular and mitral cell odor response subspaces sorted in descending order with respect to the amount variance explained by their corresponding principal vectors (PCs) in the two subspaces (these are the vectors between which the Jordan angles are calculated); the PCs that together account for 90% of the variance were included. The black trace corresponds to principal angles between random subspaces embedded in the same 49 dimensions. Different shades of green and gray correspond to principal angles between the glomerular subspace and a noise-added version of itself; varying amounts of known noise were added to the glomerular responses to change the SNR; note that adding increasing amounts of noise resulted in higher value principal angles.

is flat, and significantly fewer dimensions may be needed if a curved manifold is used to fit the data^{5,48}.

We note that the responses of MTCs are higher in dimensionality than those of glomeruli (24D versus 21D; Supplementary Fig. 4f). This could be a signature of the integration by MTCs of lateral signals across glomeruli that are not available to optical imaging on the dorsal surface, as well as of differences in sensitivity of the imaging methods used. In addition, local inhibitory inter-glomerular cross-talk, top-down feedback and neuromodulatory input may amplify the dimensionality of MTC responses, which is consistent with previous work^{20,33–36}.

The relationship between molecular properties and neuronal responses in the bulb. Using PCX analysis, we found that the PC spaces of properties and responses share little overlap. Thus, both glomeruli and MTC responses appear to include information that is not related to odor molecular properties per se. Such information may reflect valence, previous experience and expectations, or behavioral information, including changes in stimulus sampling. Additional relevant properties (not included in the set of 1,666) could also drive the responses of the olfactory neurons. The dimensionality of molecular properties increased with the number of odorants used, which is an indication of under-sampling the physical–chemical odor space (Supplementary Fig. 4f). Including ROIs from other aspects of the bulb, in addition to the dorsal surface, may strengthen this relationship. Finally, neuronal responses may simply contain randomness that is unrelated to any useful signals, although the measured variability of responses to individual odors was less than 10%. Future experiments with mice engaged in behavioral tasks, together with extended sampling of neuronal responses and further probing of the chemical space, will help disambiguate these possibilities.

Can odor properties predict OB odor responses? Several studies have suggested that the odorant molecular properties can be used to predict the responses of neurons in the olfactory system. We addressed this question for both OB inputs and outputs by asking whether similarity in molecular properties of pairs of odors can predict the similarity of neuronal population activity. We used a sparsening procedure (LASSO) that helps select the molecular properties that are most predictive of the neuronal responses. Approximately ten properties were sufficient to establish a substantial correlation (~ 0.60) between pairwise odor distances in molecular properties and similarity in neuronal population responses. To test the robustness of this relationship, we employed cross-validation methods (Fig. 2; Supplementary Figs. 4 and 5) that rigorously separated testing from training data. We found that the properties that were predictive of similarity of either glomerular or MTC responses using training odor sets failed to generalize to new pairs of odors.

Our results differ from other published studies that found predictable relations between odorant molecular properties and activity in the early stages of the olfactory system in insects, fish, tadpoles and rodents^{11,12,49} (but see refs. ^{13,19,42}). These differences could arise due to several reasons. First, owing to the number of odors used (~ 50), the relevant properties may not have been robustly established. This seems an unlikely explanation since other studies have used similar numbers of odors and did not systematically examine different concentrations, as we did for the MTCs (Supplementary Fig. 3; Methods). A second possibility is that previous analyses focused primarily on relating physical–chemical odor space to patterns of activity in the anesthetized preparations. Any relation between molecular properties and activity could be modulated by brain state. However, our experiments indicate that molecular properties explain a similarly low fraction in the variance of glomerular responses in both awake and anesthetized animals (Supplementary Fig. 5a–d). A third possibility, is that previous work may suffer from

this same problem of overfitting and poor generalization, but the regression models were not tested using pairs of odors outside the training set. We also note that the relationship of olfactory neuron responses to these physical properties could be complex and highly nonlinear, and the algorithms used here may not capture it well.

Beyond a look-up table of physical–chemical properties. There has been considerable debate regarding whether there is a continuous and recognizable map of chemical space in the OB. Since microscopy offers spatial information, we asked whether the location of glomeruli or MTCs is related to their selectivity to molecular properties. Significant correlation between odor spectra (and Dragon properties) and the location of glomeruli was observed over a broad scale (~ 4 – 5 glomerular spacings; Fig. 3). This is consistent with previous reports^{19,25,41}, which identified large chemotopic domains on the bulb surface (~ 1 mm). The precision of these predictions is substantially lower (~ 5 – 8 -fold) compared with the precision of the glomerular spatial layout across individuals (~ 0.5 – 1.0 glomerular spacings)¹⁹ (but see ref. ⁵⁰). The orientation of the identified principal axis (PC1) may reflect specific interactions between the axon terminals of OSNs and gradients of axon guidance molecular cues during the formation of the glomerular map.

With respect to the predictive power of molecular properties on glomeruli placement, the results of the regression analysis should be subject to caution given the large number of Dragon properties tested. Indeed, shuffled controls (obtained by randomizing the identity of molecular properties) produced statistically indistinguishable outcomes in the prediction of glomerular positions when using shuffled property responses along newly computed PC1 and PC2 axes.

While tiling the dorsal aspect of the bulb, we used smaller FOVs for monitoring the activities of MTCs. This constrains our conclusions on the spatial tuning of OB output neurons to properties to a finer scale (~ 0.5 mm). Weak, but significant, correlations between molecular properties and the location of somata were present only in a small number of FOVs. These correlations appear to be induced mainly by the presence of cells with highly correlated odor tuning, putative co-glomerular ‘sister’ cells⁴³, that display similar average odor tuning. When redundancies in responses were removed, any correlations between molecular properties and MTCs placement were lost (Fig. 4).

Relating the glomerular and MTC odor response spaces. Although ideally this problem should be addressed by observing MTC and glomerular responses simultaneously in the same preparation, and with same activity sensors, obtaining such data was beyond the scope of the current study. Instead, we took advantage of data acquired in different animals to determine whether the spaces sampled by the two olfactory processing layers differ in a systematic fashion. We found that populations of glomeruli and MTCs on the dorsal aspect of the bulb sample different subspaces with respect to the same panel of odors. In agreement with previous work^{30,33,45}, our analyses (PCX and CCA; Fig. 5) indicate that MTCs do not simply relay the glomerular inputs to higher olfactory centers, but substantially modify and diversify the OR input channels, as indicated by their higher dimensionality. Our data are consistent with a scenario in which glomeruli and mitral cell responses occupy intersecting, but distinct, sensory odor spaces. Their different representations may reflect feedforward input from the olfactory epithelium, local bulbar processing and top-down input, which could sample information along different axes of the odor scenes. For example, MTCs may filter out certain features of glomerular activity, but also integrate information that appears under-represented at the glomerular level. A rotation transform across odor responses relates well these two spaces (Fig. 5). This observation provides a potential framework for understanding the bulb input–output function in future

studies aimed at probing glomerular and MTC activity simultaneously in naive mice or during behavior.

Our data suggest that the physical–chemical properties used by us and others are not sufficient to fully represent the responses of olfactory bulb neurons. It seems that the molecular properties initially generated for computational chemistry studies do not capture stimulus features that are important for the sensory perception of animals, and novel descriptors are needed to link chemical space to neuronal representations. Relevant descriptors may carry information pertaining to behaviorally relevant properties of odors encountered by animals in their ecological niche as previously proposed (that is, hedonic value, edibility and survival)^{5,8,16}. Systematic exploration of the natural odor statistics may offer further insight into the structure of odor space.

Online content

Any methods, additional references, Nature Research reporting summaries, source data, statements of code and data availability and associated accession codes are available at <https://doi.org/10.1038/s41593-019-0442-z>.

Received: 14 March 2018; Accepted: 30 May 2019;

Published online: 22 July 2019

References

- Kaas, J. H. Topographic maps are fundamental to sensory processing. *Brain Res. Bull.* **44**, 107–112 (1997).
- Amoore, J. E., Palmieri, G. & Wanke, E. Molecular shape and odour: pattern analysis of PAPA. *Nature* **216**, 1084–1087 (1967).
- Bushdid, C., Magnasco, M. O., Vosshall, L. B. & Keller, A. Humans can discriminate more than 1 trillion olfactory stimuli. *Science* **343**, 1370–1372 (2014).
- Haddad, R., Lapid, H., Harel, D. & Sobel, N. Measuring smells. *Curr. Opin. Neurobiol.* **18**, 438–444 (2008).
- Koulakov, A. A., Kolterman, B. E., Enikolopov, A. G. & Rinberg, D. In search of the structure of human olfactory space. *Front. Syst. Neurosci.* **5**, 65 (2011).
- Meister, M. On the dimensionality of odor space. *eLife* **4**, e07865 (2015).
- Schiffman, S. S. Physicochemical correlates of olfactory quality. *Science* **185**, 112–117 (1974).
- Su, C.-Y., Menuz, K. & Carlson, J. R. Olfactory perception: receptors, cells, and circuits. *Cell* **139**, 45–59 (2009).
- Zarzo, M. & Stanton, D. T. Understanding the underlying dimensions in perfumers' odor perception space as a basis for developing meaningful odor maps. *Atten. Percept. Psychophys.* **71**, 225–247 (2009).
- Tetko, I. V. et al. Virtual computational chemistry laboratory—design and description. *J. Comput. Aided Mol. Des.* **19**, 453–463 (2005).
- Haddad, R. et al. A metric for odorant comparison. *Nat. Methods* **5**, 425–429 (2008).
- Haddad, R. et al. Global features of neural activity in the olfactory system form a parallel code that predicts olfactory behavior and perception. *J. Neurosci.* **30**, 9017–9026 (2010).
- Ma, L. et al. Distributed representation of chemical features and tonotopic organization of glomeruli in the mouse olfactory bulb. *Proc. Natl Acad. Sci. USA* **109**, 5481–5486 (2012).
- Saito, H., Chi, Q., Zhuang, H., Matsunami, H. & Mainland, J. D. Odor coding by a mammalian receptor repertoire. *Sci. Signal.* **2**, ra9 (2009).
- Keller, A. & Vosshall, L. B. Olfactory perception of chemically diverse molecules. *BMC Neurosci.* **17**, 55 (2016).
- Secundo, L., Snitz, K. & Sobel, N. The perceptual logic of smell. *Curr. Opin. Neurobiol.* **25**, 107–115 (2014).
- Barlow, H. B. Summation and inhibition in the frog's retina. *J. Physiol.* **119**, 69–88 (1953).
- Mombaerts, P. Axonal wiring in the mouse olfactory system. *Annu. Rev. Cell Dev. Biol.* **22**, 713–737 (2006).
- Soucy, E. R., Albeanu, D. F., Fantana, A. L., Murthy, V. N. & Meister, M. Precision and diversity in an odor map on the olfactory bulb. *Nat. Neurosci.* **12**, 210–220 (2009).
- Cleland, T. A. Early transformations in odor representation. *Trends Neurosci.* **33**, 130–139 (2010).
- Mori, K. & Sakano, H. How is the olfactory map formed and interpreted in the mammalian brain? *Annu. Rev. Neurosci.* **34**, 467–499 (2011).
- Murthy, V. N. Olfactory maps in the brain. *Annu. Rev. Neurosci.* **34**, 233–258 (2011).
- Bozza, T., McGann, J. P., Mombaerts, P. & Wachowiak, M. In vivo imaging of neuronal activity by targeted expression of a genetically encoded probe in the mouse. *Neuron* **42**, 9–21 (2004).
- Uchida, N., Takahashi, Y. K., Tanifuji, M. & Mori, K. Odor maps in the mammalian olfactory bulb: domain organization and odorant structural features. *Nat. Neurosci.* **3**, 1035–1043 (2000).
- Johnson, B. A. & Leon, M. Chemotopic odorant coding in a mammalian olfactory system. *J. Comp. Neurol.* **503**, 1–34 (2007).
- Burton, S. D. & Urban, N. N. Greater excitability and firing irregularity of tufted cells underlies distinct afferent-evoked activity of olfactory bulb mitral and tufted cells. *J. Physiol.* **592**, 2097–2118 (2014).
- Fukunaga, I., Berning, M., Kollo, M., Schmaltz, A. & Schaefer, A. T. Two distinct channels of olfactory bulb output. *Neuron* **75**, 320–329 (2012).
- Igarashi, K. M. et al. Parallel mitral and tufted cell pathways route distinct odor information to different targets in the olfactory cortex. *J. Neurosci.* **32**, 7970–7985 (2012).
- Nagayama, S., Takahashi, Y. K., Yoshihara, Y. & Mori, K. Mitral and tufted cells differ in the decoding manner of odor maps in the rat olfactory bulb. *J. Neurophysiol.* **91**, 2532–2540 (2004).
- Otazu, G. H., Chae, H., Davis, M. B. & Albeanu, D. F. Cortical feedback decorrelates olfactory bulb output in awake mice. *Neuron* **86**, 1461–1477 (2015).
- Amoore, J. E. Stereochemical and vibrational theories of odour. *Nature* **233**, 270–271 (1971).
- Schiffman, S. S. Contributions to the physicochemical dimensions of odor: a psychophysical approach. *Ann. NY Acad. Sci.* **237**, 164–183 (1974).
- Gschwend, O. et al. Neuronal pattern separation in the olfactory bulb improves odor discrimination learning. *Nat. Neurosci.* **18**, 1474–1482 (2015).
- Wiechert, M. T., Judkewitz, B., Riecke, H. & Friedrich, R. W. Mechanisms of pattern decorrelation by recurrent neuronal circuits. *Nat. Neurosci.* **13**, 1003–1010 (2010).
- Cleland, T. A. & Linster, C. On-center/inhibitory-surround decorrelation via intraglomerular inhibition in the olfactory bulb glomerular layer. *Front. Integr. Neurosci.* **6**, 5 (2012).
- Arevian, A. C., Kapoor, V. & Urban, N. N. Activity-dependent gating of lateral inhibition in the mouse olfactory bulb. *Nat. Neurosci.* **11**, 80–87 (2008).
- Yablonka, A., Sobel, N. & Haddad, R. Odorant similarity in the mouse olfactory bulb. *Proc. Natl Acad. Sci. USA* **109**, E2918–E2919 (2012).
- Friedman, J., Hastie, T. & Tibshirani, R. Regularization paths for generalized linear models via coordinate descent. *J. Stat. Softw.* **33**, 1–22 (2010).
- Belluscio, L. & Katz, L. C. Symmetry, stereotypy, and topography of odorant representations in mouse olfactory bulbs. *J. Neurosci.* **21**, 2113–2122 (2001).
- Friedrich, R. W. & Korsching, S. I. Combinatorial and chemotopic odorant coding in the zebrafish olfactory bulb visualized by optical imaging. *Neuron* **18**, 737–752 (1997).
- Mori, K., Takahashi, Y. K., Igarashi, K. M. & Yamaguchi, M. Maps of odorant molecular features in the mammalian olfactory bulb. *Physiol. Rev.* **86**, 409–433 (2006).
- Cleland, T. A. & Sethupathy, P. Non-topographical contrast enhancement in the olfactory bulb. *BMC Neurosci.* **7**, 7 (2006).
- Dhawale, A. K., Hagiwara, A., Bhalla, U. S., Murthy, V. N. & Albeanu, D. F. Non-redundant odor coding by sister mitral cells revealed by light addressable glomeruli in the mouse. *Nat. Neurosci.* **13**, 1404–1412 (2010).
- Maaten, L. vander & Hinton, G. Visualizing data using t-SNE. *J. Mach. Learn. Res.* **9**, 2579–2605 (2008).
- Linster, C. & Cleland, T. A. Neuromodulation of olfactory transformations. *Curr. Opin. Neurobiol.* **40**, 170–177 (2016).
- Fantana, A. L., Soucy, E. R. & Meister, M. Rat olfactory bulb mitral cells receive sparse glomerular inputs. *Neuron* **59**, 802–814 (2008).
- Björck, Åke & Golub, G. H. Numerical methods for computing angles between linear subspaces. *Math. Comp.* **27**, 579–594 (1973).
- Zhou, Y., Smith, B. H. & Sharpee, T. O. Hyperbolic geometry of the olfactory space. *Sci. Adv.* **4**, eaq1458 (2018).
- Wang, G., Carey, A. F., Carlson, J. R. & Zwiebel, L. J. Molecular basis of odor coding in the malaria vector mosquito *Anopheles gambiae*. *Proc. Natl Acad. Sci. USA* **107**, 4418–4423 (2010).
- Zapiec, B. & Mombaerts, P. Multiplex assessment of the positions of odorant receptor-specific glomeruli in the mouse olfactory bulb by serial two-photon tomography. *Proc. Natl Acad. Sci. USA* **112**, E5873–E5882 (2015).

Acknowledgements

The authors would like to acknowledge members of the Albeanu and Koulakov labs and F. Carnevale for critical discussions, and M. Davis and R. Eifert for technical support. This work was supported by the following funding sources: BBRF 2014 Young Investigator grant to H.C.; WSBS PhD support to D.R.K.; Swartz Fellowship to W.G.B.;

R01DC014366 to A.A.K.; NSF IOS-1656830 and NIH R01DC014487-03 to D.F.A.; and R01DC017876-01 to A.A.K. and D.F.A.

Author contributions

D.F.A. and A.A.K. conceived the study. H.C., D.R.K., W.G.B., A.A.K. and D.F.A. contributed to the design of experiments and analyses. H.C. performed the two-photon imaging experiments. W.G.B. performed the intrinsic optical imaging experiments. D.F.A., V.N.M. and A.A.K. supervised the project and wrote the manuscript with input from all authors.

Competing interests

The authors declare no competing interests.

Additional information

Supplementary information is available for this paper at <https://doi.org/10.1038/s41593-019-0442-z>.

Reprints and permissions information is available at www.nature.com/reprints.

Correspondence and requests for materials should be addressed to A.A.K. or D.F.A.

Peer review information: *Nature Neuroscience* thanks Nathan Schoppa and the other, anonymous, reviewer(s) for their contribution to the peer review of this work.

Publisher's note: Springer Nature remains neutral with regard to jurisdictional claims in published maps and institutional affiliations.

© The Author(s), under exclusive licence to Springer Nature America, Inc. 2019

Methods

Chronic windows for awake, head-fixed intrinsic and multiphoton imaging.

Adult B6/129 (8 females and 1 male, >80 days old, 25–40 g) and TBET-Cre X Ai38 GCaMP3.0 (4 males and 4 females, >80 days old, 25–40 g) or Ai 95 GCaMP6f mice (3 males, >80 days old, 25–40 g) were anesthetized with ketamine/xylazine (initial dose 70/7 mg per kg), supplemented every 45 min. Heart beat, respiratory rate and lack of pain reflexes were monitored throughout the procedure. Animals were administered dexamethasone (1 mg per kg) to prevent swelling, enrofloxacin (5 mg per kg) to protect against bacterial infection and carprofen (5 mg per kg) to reduce inflammation. To expose the dorsal surface of the OB for chronic imaging, a small craniotomy was made over both OB hemibulbs, using either a biopsy punch⁵¹ or thinning the skull with a 27 high-speed dental drill (Foredom) and removing it completely. A 3-mm glass cover slip (CS-3R, Warner Instruments) was placed on top and sealed in place using Vetbond (3M), further reinforced with cyanoacrylate (Krazy Glue) and dental acrylic (Lang Dental). A custom-built titanium head-bar was cemented on the skull near the lambda suture as previously described^{26–30}. Carprofen (5 mg per kg) was administered for 2 days following surgery. Animals were left to recover for at least 48 h after surgery before imaging and further habituated before the imaging sessions. All animal procedures conformed to NIH guidelines and were approved by the Animal Care and Use Committee of Cold Spring Harbor Laboratory.

Odor stimulation. A custom odor delivery machine was built to automatically deliver up to 165 stimuli and in any desired sequence under computer control of solenoid valves (AL4124 24 VDC, Industrial Automation Components). Pure chemicals and mixtures were obtained from Sigma and from International Flavors and Fragrances. Odorants were diluted 1:3,000 and 1:100 in mineral oil and placed in blood collection tubes (Vacutainer, no. 366431) loaded on a custom-made rack and sealed with a perforated rubber septum circumscribing two blunt-end needles (Mcmaster, no. 75165A754). Fresh air was pumped into each tube via one needle by opening the corresponding solenoid valve. The mixed odor stream exited the tube through the other needle and was delivered at $\sim 1 \text{ l min}^{-1}$ via Teflon-coated tubing to the animal's snout. The concentration of the odors delivered to the mouse was measured using a photo-ionization device (PID; Aurora Scientific) and found to range between ~ 0.05 and 1% saturated vapor pressure. The same PID was used to determine the time course of the odor waveform and the reliability of odor stimulation. A list of odors used in our experiments is provided in Supplementary Table 1. A total of 49 out of the 57 stimuli used were monomolecular compounds, and were further included in the physical–chemical properties analysis. For the comparison of glomerular and MTC responses, the 1:100 dilution was used for the same 49 odors. In a set of six MTC FOVs (three mice), only the first 33 odors in the panel were used.

In general, for intrinsic optical imaging experiments, in each stimulus trial, we presented 12 s of air followed by 24 s of odor delivery. The interval between trials was at least 45 s, and each stimulus was repeated 4–5 times. Data were obtained from nine mice (five awake female mice, ten bulb hemispheres = hemibulbs, and four mice (one male, three females), eight hemibulbs, for which responses were sampled in both awake and anesthetized states). For two-photon experiments, we scanned at 5–10 Hz per frame and covered a FOV up to $\sim 350 \times 500 \mu\text{m}$ in the MTC layers. Before delivering odors, the OB was examined to gauge the quality of the surgery and to select the ROIs. The resting fluorescence of GCaMP3/6 (refs. ^{52,53}) is low, but could be discerned by frame averaging (approximately ten frames). Resting images at different depths were obtained before choosing specific optical sections for further experiments. Once a specific optical section was chosen, a time sequence of 120–240 frames was acquired. During the first 10 s, fresh air was delivered, followed by odor stimuli (of a matched flow rate to the fresh air to avoid mechanical olfactory sensory neuron activation) for 4 s. Finally, fresh air was delivered for 10 s. The inter-trial interval was 45 s. Each odor was typically delivered 3–4 times.

Intrinsic and multiphoton imaging. We used computer controlled light-emitting diodes to shine far-red light (780 nm) for imaging intrinsic optical signals, which are a good proxy for presynaptic OSN activity^{19,54,55}, on the dorsal surface of the bulb, acquiring images at 25 Hz (Vosskuhler, 1300-QF CCD camera). For two-photon imaging, we used a Chameleon Ultra II Ti:sapphire femtosecond pulsed laser (Coherent) and a custom-built multiphoton microscope. The shortest possible optical path was used to bring the laser onto a galvanometric mirrors scanning system (6215HB, Cambridge Technologies). The scanning system projected the incident laser beam tuned at 930 nm through a scan lens and tube lens to backfill the aperture of an Olympus $\times 20$, 1.0 NA objective. Scanning and acquisition were performed using custom Labview-based software (National Instruments).

Imaging odor responses in MTCs of the OB. We used resting fluorescence and the presence of dark nuclei to identify tufted or mitral cells in the imaged field (Supplementary Fig. 1d,f). We observed robust odor responses in the cell bodies of both tufted cells, identified on the basis of the location of their somata in the external plexiform layer (Supplementary Fig. 1d,e) and mitral cells (Supplementary Fig. 1f,g). Different odors led to different spatial (Supplementary Fig. 1d,f) and

temporal (Supplementary Fig. 1e,g) patterns of activation of MTCs. Responses to a given odor had diverse amplitudes and time courses in different cells (Supplementary Fig. 1d–g). Conversely, a given cell responded to different odors with distinct amplitude and temporal dynamics and showed low trial-to-trial variability (Supplementary Fig. 1e,g).

For each cell type, we calculated the mean fluorescence change during odor presentation and obtained an odor response spectrum or odor tuning curve for 55 odors (of which 53 were monomolecular; Supplementary Table 1) per imaging session (Supplementary Fig. 1d,g). As observed in the example odor response spectrum shown, different tufted (Supplementary Fig. 1e) and mitral cells (Supplementary Fig. 1g) responded in a distinctive manner to the odors used. Measurements of the odor waveform using a PID indicated that the temporal diversity of responses across odors was not due to differences in stimulus kinetics (data not shown).

To test our results across a range of concentrations, we used two different oil dilutions (1:3,000 and 1:100) of each odor and sampled the responses of MTCs in 19 different FOVs tiling the dorsal surface aspect of the bulb (out of these, for six FOVs, both dilutions were sampled). PID measurements of five randomly sampled odors indicated that these dilutions roughly span a range of 18 ± 5 -fold in concentration (Supplementary Fig. 2a). Clustering responses based on their temporal dynamics (hierarchical clustering) showed that sustained excitatory responses, as well as inhibitory responses, were more frequent in mitral cells than in tufted cells (Supplementary Fig. 2c,d).

Data analyses. For the intrinsic imaging experiments, responsive glomeruli were identified as previously described¹⁹. For MTCs, ROIs were manually selected based on anatomy. Care was taken to avoid selecting ROIs on cell bodies overlapping with neuropil (MTC lateral dendrites). To facilitate the detection of responding cells or regions, we calculated a ratio image for each odor (the average of images in the odor period minus the average of images in the pre-stimulus period, normalized by the pre-stimulus average). We further obtained a maximum pixel projection of all odor responses, assigning to each pixel in the FOV the maximum response amplitude across the odor panel used, which allowed us to visually identify odor-responsive regions. These responsive ROIs mapped to individual mitral or tufted cell bodies in the fluorescence image and were selected for further analyses¹⁹.

Statistics. All analyses were performed using Matlab (Mathworks) and Igor (Wavemetrics). The following analyses were performed: paired *t*-test, FDR correction, analysis of variance (ANOVA) and signed-rank test. All tests were two-sided unless otherwise noted. For parametric tests, the data distribution was assumed to be normal, but this was not formally tested. No statistical methods were used to predetermine sample sizes, but our sample sizes were similar to those reported in previous publications^{19,24,43}. Randomization of conditions was not relevant to the study, and data collection and analyses were not performed blinded to the conditions of the experiments.

Odor responses. To obtain odor responses, we computed the average fluorescence during the period of odor presentation for each trial i , F_{2i} , and the average fluorescence during the preceding air period F_{1i} . Responses were defined as significant for $P < 0.1$ (two-way ANOVA). Because additional more stringent statistical tests were performed in the subsequent analyses, we reasoned that preliminary filtering of the data at the level of $P < 0.1$ is reasonable. For the subsequent analyses, we used the relative response (dF/F) defined as follows:

$$\Delta_{cs} = \overline{(F_{2st} - F_{1st})} / F_{1st} \quad (2)$$

where the indexes c , s and t enumerate ROIs (that is, cells), odors and trials respectively, while the average is computed over the trials i .

For intrinsic optical imaging of glomeruli, we applied the same procedure as previously described¹⁹. Control ROIs drawn in nonresponsive areas of the bulb were used to obtain a response signal threshold by comparing the odor responses in an equal number of active glomeruli. Varying a signal threshold, the number of control ROIs that passed the threshold was compared with the number of responses in regions identified as active glomeruli to obtain a false positive ratio of < 0.1 . For both glomeruli and MTCs, ROI–odor pairs with nonsignificant responses were set to 0.

Hierarchical clustering. To identify mitral cell bodies with similar odor tuning (that is, putative co-glomerular sister cells)^{43,56,57}, we performed a cluster analysis based on the similarity between odor response spectra (average linkage, cut-off = 0.7). Each cluster with three or more members was taken to represent potential sister MTCs receiving common primary input from the same parent glomerulus and considered for further analysis.

Odor physical–chemical property response and property response spectra. To determine the sensitivity of individual ROIs to various properties, we evaluated the property response spectra, Φ_p , which are the chemical receptive fields of the ROIs. Each element of the matrix Φ_p with indexes c and p indicates the strength of response of a given ROI, c , to an odor physical–chemical property, p . Thus,

the matrix Φ_p describes the physical–chemical tuning of the set of ROIs. To compute Φ_p , we first calculated the values of 1,666 physical–chemical properties for the odors used in our panel. This resulted in a property matrix P_{sp} . The index s enumerates the monomolecular odors (1–53 for MTCs and 1–49 for glomeruli), as described above, while the second index p , ranging between 1 and 1,666, denotes the physical–chemical properties. The property matrix was obtained by downloading molecular structures for the monomolecular odors from PubChem and using an online set of algorithms from Dragon to evaluate the physical–chemical properties. The full list of molecular descriptors (physical–chemical properties) used can be found at: http://www.talete.mi.it/products/dragon_molecular_descriptor_list.pdf.

Because the obtained properties were highly inhomogeneous in ranges and scales, we normalized the data as outlined below. If a property took both negative and positive values for the odors in the panel, we subtracted the mean value for this property and divided by the standard deviation across the odors in the panel. If a property was strictly positive (for example, molecular weight), we examined the standard deviation of its logarithm (SDL). If the SDL was larger than 1, we assumed that the property is lognormally distributed. The corresponding property was replaced in matrix P_{sp} by its logarithm with the mean subtracted. If the SDL was smaller than 1, we subtracted the mean from the property and divided the values by its standard deviation for the odors in the panel. Normalizing each property by the standard deviation, we minimized the influence of measurement units on the dynamic range of some properties, which could introduce a subjective bias. By implementing this procedure, all properties were brought to zero mean and similar standard deviations. The resulting matrix was denoted \tilde{P}_{sp} . Approximately 300 physical–chemical properties did not take non-zero values for the odors in our panel, and were therefore not included in the analysis.

To compute the property response spectrum, the chemical receptive field of a ROI across the properties, we used the following formula:

$$\Phi_{cp} = \sum_s \tilde{\Delta}_{cs} \tilde{P}_{sp} \quad (3)$$

For each ROI, c , a property response, defined as an entry in the property response spectrum, was equal to the correlation between the dF/F odor responses (normalized to the unit standard deviation) of this ROI and the normalized PSV, given by the values taken by property p computed over the entire set of odors presented (enumerated by s).

To evaluate the significance of the correlation between a property and the response pattern of a ROI, we use a P value threshold of 0.05. P values were calculated using Matlab's built-in function `corr()`. This implementation evaluates the t statistic as $t = \frac{r\sqrt{n-2}}{\sqrt{1-r^2}}$, where r is the correlation coefficient and n is the number of data points. The P value is then twice the probability a t -distributed variable exceeds t . We also applied FDR correction³⁸ for the property response spectrum of each ROI at $q < 0.1$.

Odorant response similarity and property space similarity. We computed the correlation matrix of the relative responses (dF/F) Δ_{cs} and Δ_{ck} between each pair of odors, s and k , for all glomeruli or cells, c as follows:

$$C_{sk} = \frac{\sum_c (\Delta_{cs} - \bar{\Delta}_s)(\Delta_{ck} - \bar{\Delta}_k)}{\sqrt{\sum_c (\Delta_{cs} - \bar{\Delta}_s)^2} \sqrt{\sum_c (\Delta_{ck} - \bar{\Delta}_k)^2}} \quad (4)$$

Where $\bar{\Delta}_k = \frac{1}{N} \sum_{c=1}^N \Delta_{ck}$. Indexing the unique pairs of odors of C_{sk} with i , we have a vector of correlations, \tilde{C}_i . Using the property matrix \tilde{P}_{sp} described above, we calculated the Euclidean distance matrix as follows:

$$D_{sk} = \sqrt{\sum_p (\tilde{P}_{sp} - \tilde{P}_{kp})^2} \quad (5)$$

We calculated the Euclidean distances of the neuronal response space between each odor s and k as $N_{sk} = \sqrt{\sum_c (\Delta_{cs} - \Delta_{ck})^2}$. \tilde{N}_i is the vectorized unique odor pairs of N_{sk} . Figure 2a,b (upper) plots \tilde{D}_i against \tilde{N}_i . Following the same vectorization procedure as for the response correlations \tilde{C}_i , we vectorized the unique pairs of odors in matrix D_{sk} with \tilde{D}_i . Figure 2a,b (lower) shows a plot of \tilde{D}_i versus \tilde{C}_i .

We searched for a subset of properties that generate property distances \tilde{D}_i^2 that correlate best with neuronal response distances \tilde{N}_i^2 . For this, we used the LASSO algorithm³⁸. This algorithm minimizes the following equation:

$$\lambda \sum_p |\beta_p| + \left(\sum_i \left(\sum_c (\Delta_{cs} - \Delta_{ck})^2 \right)_i - \left(\sum_p \beta_p (\tilde{P}_{sp} - \tilde{P}_{kp})^2 \right)_i \right)^2 \quad (6)$$

Where $(\cdot)_i$ denotes the vectorization of the unique pairs of odors s and k described above. Manipulating each weight β_p (non-negative) to minimize the term $\left(\sum_i \left(\sum_c (\Delta_{cs} - \Delta_{ck})^2 \right)_i - \left(\sum_p \beta_p (\tilde{P}_{sp} - \tilde{P}_{kp})^2 \right)_i \right)^2$ creates a property space with square property distances $D_{sk}^2 = \sum_p \beta_p (\tilde{P}_{sp} - \tilde{P}_{kp})^2$ that reconstruct the square neuronal response distances $N_{sk}^2 = \sum_c (\Delta_{cs} - \Delta_{ck})^2$. The first term of the LASSO objective function, $\sum_p |\beta_p|$, penalizes the use of non-zero weights (Supplementary

Fig. 4i). This forces the algorithm to choose the most parsimonious property space to reconstruct the neuronal response space. Increasing the parameter λ puts more pressure on each β_p to be zero. Figure 3c,d shows, for different numbers of non-zero properties, the correlations between distances in the weighted property space $\left(\sum_p \beta_p (\tilde{P}_{sp} - \tilde{P}_{kp})^2 \right)_i$ and distances in the neuronal response space $\left(\sum_c (\Delta_{cs} - \Delta_{ck})^2 \right)_i$.

If all molecular property weights had values of 1, using LASSO, one would arrive at the correlation values shown in Fig. 2a,b. To find a sparse and robust solution, the LASSO algorithm assigns zero value to the weights of most molecular properties. By varying a penalty parameter (λ) of the algorithm (Supplementary Fig. 4i), we changed the number and relative contribution of the molecular properties included in computing the pairwise odor distances.

To cross-validate new responses, we randomly selected and withheld half of the FOVs and performed LASSO regression on the remaining data (training set). Then, we recomputed the correlations between property distance and response distance in the withheld data (testing set).

To determine how our results generalized for new stimuli, we removed one pair of odors from the panel (jackknife, leave one out) and performed the above analysis on the rest of the data. Then we calculated the distance between the two removed odors in the reduced property space found by LASSO regression. We repeated this procedure independently for each pair of odors i , with each repetition generating one property distance $\left(\sum_p \beta_p (\tilde{P}_{sp} - \tilde{P}_{kp})^2 \right)_i$. Then, we found the correlation between the vector of these property distances and the neuronal response distances $\left(\sum_c (\Delta_{cs} - \Delta_{ck})^2 \right)_i$. Thus, every prediction of an odor pair similarity was obtained based only on the odor similarities calculated for all other odor pairs.

Finally, we cross-validated new FOVs and new odors by combining the two previous cross-validation procedures. That is, we withheld one pair of odors and half of the FOVs, and then performed LASSO. Using the reduced property space found by LASSO, we then predicted the response distance of the two removed odors in the withheld response data.

The physical–chemical properties selected by LASSO regression were different for the cross-validated and non-cross-validated curves presented in Fig. 2. This is because the data available in each case were different. For FOV cross-validation, a different set of properties emerged for each subset of selected FOVs in the training set. Similarly, for odor cross-validation, the distance between each pair of odors was calculated using a different data subset and led to distinct sets of best properties.

Greedy algorithm. First, we found the property for which the Euclidean distance of each pair of odorants best correlated with the odor response similarity, which was defined as the correlation between the mitral or tufted cell neuronal response profiles (cell response spectra) in all the FOVs of these two odorants. Second, we searched through all remaining properties, and with each iteration added to the metric the property that most greatly increased the correlation between the physical–chemical property distance and the neuronal response odor similarity. The process terminated once the addition of any new property decreased the correlation (Supplementary Fig. 4j).

Correlations between ROI property response spectra and ROI locations.

To evaluate the physical–chemical property and position correlations, we computed the Pearson's correlation coefficients between the locations of ROIs $\tilde{r}_c = (x_c, y_c)$ and their property response spectra (receptive fields, Φ_p). Here x_c and y_c are AP and ML positions, respectively, of a ROI k on the surface of the bulb. If the average locations are $\bar{x} = \frac{1}{N} \sum_{c=1}^N x_c$ and $\bar{y} = \frac{1}{N} \sum_{c=1}^N y_c$, the Pearson's correlation for a property p with the position of the ROI along the AP axis is defined as follows:

$$R_{xp} = \frac{\sum_c (x_c - \bar{x})(\Phi_{cp} - \bar{\Phi}_p)}{\sqrt{\sum_c (x_c - \bar{x})^2} \sqrt{\sum_c (\Phi_{cp} - \bar{\Phi}_p)^2}} \quad (7)$$

where $\bar{\Phi}_p = \frac{1}{N} \sum_{c=1}^N \Phi_{cp}$. Similarly, the correlation of the property to ML position, denoted as y , is defined as follows:

$$R_{yp} = \frac{\sum_c (y_c - \bar{y})(\Phi_{cp} - \bar{\Phi}_p)}{\sqrt{\sum_c (y_c - \bar{y})^2} \sqrt{\sum_c (\Phi_{cp} - \bar{\Phi}_p)^2}} \quad (8)$$

In addition to calculating the correlation values, we evaluated their statistical significance using the Matlab function 'corr'. The corresponding P values were computed for each property: P_{xp} and P_{yp} . We applied FDR correction³⁸ to each set of P values and found the set of q values Q_{xp} and Q_{yp} using the Matlab function 'mafdr'. A property was assumed to be significantly correlated with AP or ML axes if the corresponding q value was less than 0.1. The properties with significant correlations are shown in Fig. 4a,b by color.

Predictions of glomerular position based on odor physical–chemical properties.

We tested whether the tuning properties of glomeruli are predictive of their locations in the bulb. Different sets of properties were selected such as to yield the best match of glomerular positions for each FOV and reference axes

(PC1 versus PC2). To this end, for each FOV and for each bulb axis, we built a linear regression that should approximate the positions of glomeruli, c :

$$x_c = \sum_p \Phi_p W_{xp} \tag{9}$$

$$y_c = \sum_p \Phi_p W_{yp} \tag{10}$$

where W_{xp} and W_{yp} are sparse vectors of unknown coefficients that were found using the LASSO algorithm³⁸. We added a column of ones to the matrix Φ_p to include a possible offset to the approximation of coordinates. We ensured that the vectors W_{xp} and W_{yp} have only 20 non-zero components. To validate the prediction built on the basis of glomerular receptive fields, we excluded a single ROI (glomerulus) from the dataset, further obtained regressions with the LASSO algorithm based on the remaining ROIs, and then used the removed glomerulus to test the quality of prediction (jackknife cross-validation). We repeated this procedure for all glomeruli in the dataset. We verified that changing the number of active properties did not substantially affect our results. The resulting predictions for glomerular positions were compared to the actually observed bulbar positions, and the quality of predictions was evaluated by computing the distance between actual and predicted positions measured in terms of AGS (75 μ m; Fig. 3g,h). The same analysis was performed on shuffled properties control, whereby the PSVs were shuffled by odor identity.

Dimensionality of physical–chemical properties and glomerular and MTC responses. We sampled an increasing number of monomolecular odors within our panel (up to 49) and performed PCA to calculate the dimensionality (90% variance explained) of the properties (PSV) and of the glomerular and MTC odor responses. To estimate the robustness of this analysis, for each number of odors considered, we constructed a distribution of 1,000 odor sets and sampled random combinations of the possible odor subsets within the panel (Supplementary Fig. 4f).

PCA space comparison using the PCX method. To compare the odor spaces sampled by mitral cells versus glomeruli, we projected them onto the PCs of each other. More explicitly, we considered the matrix of mitral cell responses, with element M_{ms} corresponding to a mitral cell m responding to an odor s , and similarly the response matrix with elements G_{gs} for a glomerulus g and an odor s . For each response matrix, singular value decompositions can be written as follows:

$$G = U_G D_G V_G^T, M = U_M D_M V_M^T \tag{11}$$

where $D_{G/M}$ and $V_{G/M}$ are the unitary matrix, diagonal singular value matrix and eigenvector (PC) matrix, respectively, for the glomerular and MTC response matrices. If dimensions of the matrix G are $[N_G \times N_s]$, that is, the number of glomeruli by the number of odors, the dimensions of matrices U_G , D_G and V_G are $N_G \times N_s$, $N_s \times N_s$ and $N_G \times N_s$, respectively. Here, the number of odors is smaller than the number of glomeruli. We then computed projections of mitral cell responses onto the glomerular PCs, M_G , and the projections of glomerular responses onto the mitral cell PCs, G_M , as follows:

$$G_M = G V_M, M_G = M V_G \tag{12}$$

The variance of the glomeruli projections for each mitral cell PC was calculated as follows:

$$\sigma_p^2 = \frac{\sum_g (G_{Mgp} - \mu_{Gp})^2}{N_G} \tag{13}$$

Where μ_{Gp} is mean of the glomerular responses on the mitral cell PC, p , and N_G is the total number of glomeruli. The variance for mitral cells projected onto glomeruli can be found by replacing every instance of G with M and g with m .

The random data control used in Fig. 1 is a random matrix, $N_G \times N_s$, constructed by sampling from a Gaussian distribution centered at 0 with s.d. = 1.

Re-sampling model. In this model, we tested whether mitral cell responses are a re-sampling of glomeruli responses. To obtain the responses of one MTC to the odors in our panel, we randomly selected a glomerulus in the dataset and assumed that neuronal responses faithfully relay inputs from this glomerulus. We randomly selected glomeruli with repetition to generate a new response matrix with an equal number of cells as for the true mitral cell response matrix. We then used the PCA space comparison method described above to compare the re-sampled glomeruli to the true mitral cell responses.

Rotation model. We tested whether mitral cell responses constitute a rotation of the sampling of odor space by glomeruli. Using the notation from the PCA space comparison method, we modeled surrogate mitral cell responses to be

$$\tilde{M} = GQ \tag{14}$$

Where Q is a $N_s \times N_s$ rotation matrix, calculated as follows:

$$Q = V_G V_M^T \tag{15}$$

Because $G = U_G D_G V_G^T$ and $V_G^T V_G = I$, for the surrogate mitral cell responses (equation (15)) we obtain $\tilde{M} = U_G D_G V_M^T$. We further compared the rotated glomeruli response matrix with the mitral cell response matrix using the PCA space comparison method described above.

The rotation matrix Q cannot be viewed as a connectivity matrix. This rotation does not make predictions regarding the specific connectivity of individual glomeruli and mitral cells. Instead, it enables us to compare the sampling of odor space by the two layers of the OB. This is because, in equation (15), matrix Q multiplies the glomerular responses G on the right, thus mixing the responses of glomeruli to different smells to obtain the surrogate mitral cell responses, \tilde{M} . Our model aims to relate glomerular and MTC response spaces using a minimum number of parameters.

A circuit-level model would be required to pool together inputs from multiple glomeruli (versus pooling single glomerular responses across odors) to produce MTC responses⁴⁶. To obtain a weight matrix W that mixes glomerular responses for the same odor to obtain the same surrogate matrix, \tilde{M} , one would have to multiply the glomerular matrix on the left; that is,

$$\tilde{M} = \hat{W} \cdot \hat{G} \tag{16}$$

Here, \hat{W} is the (glomeruli \times glomeruli) weight matrix, which is much larger than the matrix \hat{Q} . Because $\tilde{M} = U_G D_G V_M^T$ and $G = U_G D_G V_G^T$, the weight matrix can be identified as follows:

$$W = U_G D_G V_M^T V_G D_G^{-1} U_G^T \tag{17}$$

These two equations can be viewed as feedforward network equations that produce mitral cell responses from glomerular activities. In comparison, equation (1) yields an equivalent, albeit more compact, relationship between mitral and glomerular responses than equation (17).

Jordan principal angles. A standard method for comparing the relation between multidimensional subspaces is to calculate the Jordan principal angles between them. In CCA, the cosine of the Jordan principal angles is the canonical correlation. Intuitively, CCA identifies the two maximally correlated vectors (called principal vectors) between the pair of subspaces of interest and calculates the angle between them (Jordan principal angle). The principal vectors are PCs for their corresponding subspaces. This process is iterated to identify all other remaining maximally correlated principal vectors (with the added constraint that they have to be orthogonal to the previously identified pairs of principal vectors) and to further calculate the corresponding Jordan angles between them. For example, the relationship between two lines intersecting in a multidimensional space is described by a single Jordan angle. For planes of higher than 1D, their arrangement is described by more than one Jordan angle. For two randomly selected 2D planes, there are two Jordan angles: one angle is formed by the vectors perpendicular to these planes, and one angle that is always zero. Because 2D planes intersect along a line, the second Jordan angle is formed by two vectors belonging to two planes running along the intersection and is, consequently, zero.

For two n D planes, the number of Jordan angles is n . If these planes are embedded into an N dimensional ($N \geq n$) space ($N \geq n$), two planes placed arbitrarily with respect to each other (for example random), intersect along a space of dimension 0 if $2n \leq N$, like two lines on a 2D plane. In this case, all Jordan angles are expected to be non-zero. For example, the relative arrangement of two 5D planes in general position in a 10D space is described by five non-zero Jordan angles. For $2n > N$, at least $2n - N$ Jordan angles are zero. For example, two 2D planes in 3D form two Jordan angles, one of which is zero. The same 2D planes in 4D, however, form two Jordan angles, all of which, in general, are non-zero. Finally, for two N D planes embedded in N dimensions ($N = N$), all N Jordan angles are zero, since these planes coincide (Supplementary Fig. 8).

To calculate the Jordan principal angles between subspaces, we used the singular value decomposition (SVD) method⁴⁷. In this approach, the SVD of the Gram matrix is computed for two PC bases in each subspace, and the diagonal part of the diagonal matrix is used to identify the cosines of Jordan angles. We gradually increased the dimensionality of the two PC subspaces by using only PCs with the highest variance (until explaining 90% of variance).

PCX compared to Jordan's angles. We were not only interested in comparing dimensions but also in the variance in those dimensions. For example, we wanted to use a method that determines whether input responses are highly variant to an odorant dimension, but then lowly variant to that dimension in the output responses. Standard use of Jordan principal angles does not distinguish between these cases. To identify such cases, instead of directly computing the Jordan principal angles between the two subspaces, we first considered further subspaces of both subspaces. We then progressively included PCs of both these subspaces, iteratively re-computing the subspace principal angles for each addition.

More formally, for matrix $A \in R^{N \times M}$ and $B \in R^{P \times M}$, we computed the SVD for both $A_{nm} = \sum_{ql} U_{nq}^a S_{ql}^a V_{ml}^a$ and $B_{pm} = \sum_{ql} U_{pq}^b S_{ql}^b V_{ml}^b$. The columns and rows of these SVD matrices are ordered such that the diagonal elements of S are descending in order. Thus, the PCs of V are ordered by the amount of variance they include in descending order. Then if $\theta(x, y)$ is a function that computes the subspace angles between matrices x and y , we find $\vec{k}_i = \theta\left(\sum_{l=1}^i \sum_q U_{nq}^a S_{ql}^a V_{ml}^a, \sum_{l=1}^i \sum_q U_{nq}^b S_{ql}^b V_{ml}^b\right)$ for $i = 1 \dots M$. Because the order of the PCs of each subspace depends on the variance, some of the elements of $\vec{k}_1, \vec{k}_2 \dots \vec{k}_M$ may contain non-zero angles, indicating that the data are distinct in variance.

Reporting Summary. Further information on research design is available in the Nature Research Reporting Summary linked to this article.

Data availability

All data matrices representing glomerular and MTC odor responses and physical-chemical descriptors for the odors in the panel included in the analyses presented here are available on github at: https://github.com/TeamAlbeanu/mosaic_representations.

Code availability

The code used for analysis is available upon request.

References

- Adam, Y. & Mizrahi, A. Long-term imaging reveals dynamic changes in the neuronal composition of the glomerular layer. *J. Neurosci.* **31**, 7967–7973 (2011).
- Zariwala, H. A., Kepecs, A., Uchida, N., Hirokawa, J. & Mainen, Z. F. The limits of deliberation in a perceptual decision task. *Neuron* **78**, 339–351 (2013).
- Chen, T.-W. et al. Ultrasensitive fluorescent proteins for imaging neuronal activity. *Nature* **499**, 295–300 (2013).
- Gurden, H., Uchida, N. & Mainen, Z. F. Sensory-evoked intrinsic optical signals in the olfactory bulb are coupled to glutamate release and uptake. *Neuron* **52**, 335–345 (2006).
- Vincis, R., Lagier, S., Van De Ville, D., Rodriguez, I. & Carleton, A. Sensory-evoked intrinsic imaging signals in the olfactory bulb are independent of neurovascular coupling. *Cell Rep.* **12**, 313–325 (2015).
- Buonviso, N. & Chaput, M. A. Response similarity to odors in olfactory bulb output cells presumed to be connected to the same glomerulus: electrophysiological study using simultaneous single-unit recordings. *J. Neurophysiol.* **63**, 447–454 (1990).
- Kikuta, S., Fletcher, M. L., Homma, R., Yamasoba, T. & Nagayama, S. Odorant response properties of individual neurons in an olfactory glomerular module. *Neuron* **77**, 1122–1135 (2013).
- Benjamini, Y. & Hochberg, Y. Controlling the false discovery rate—a practical and powerful approach to multiple testing. *J. R. Stat. Soc. Ser. B* **57**, 289–300 (1995).

Reporting Summary

Nature Research wishes to improve the reproducibility of the work that we publish. This form provides structure for consistency and transparency in reporting. For further information on Nature Research policies, see [Authors & Referees](#) and the [Editorial Policy Checklist](#).

Statistics

For all statistical analyses, confirm that the following items are present in the figure legend, table legend, main text, or Methods section.

n/a Confirmed

- | | | |
|-------------------------------------|-------------------------------------|--|
| <input type="checkbox"/> | <input checked="" type="checkbox"/> | The exact sample size (n) for each experimental group/condition, given as a discrete number and unit of measurement |
| <input type="checkbox"/> | <input checked="" type="checkbox"/> | A statement on whether measurements were taken from distinct samples or whether the same sample was measured repeatedly |
| <input type="checkbox"/> | <input checked="" type="checkbox"/> | The statistical test(s) used AND whether they are one- or two-sided <i>Only common tests should be described solely by name; describe more complex techniques in the Methods section.</i> |
| <input type="checkbox"/> | <input checked="" type="checkbox"/> | A description of all covariates tested |
| <input type="checkbox"/> | <input checked="" type="checkbox"/> | A description of any assumptions or corrections, such as tests of normality and adjustment for multiple comparisons |
| <input type="checkbox"/> | <input checked="" type="checkbox"/> | A full description of the statistical parameters including central tendency (e.g. means) or other basic estimates (e.g. regression coefficient) AND variation (e.g. standard deviation) or associated estimates of uncertainty (e.g. confidence intervals) |
| <input type="checkbox"/> | <input checked="" type="checkbox"/> | For null hypothesis testing, the test statistic (e.g. F , t , r) with confidence intervals, effect sizes, degrees of freedom and P value noted <i>Give P values as exact values whenever suitable.</i> |
| <input checked="" type="checkbox"/> | <input type="checkbox"/> | For Bayesian analysis, information on the choice of priors and Markov chain Monte Carlo settings |
| <input checked="" type="checkbox"/> | <input type="checkbox"/> | For hierarchical and complex designs, identification of the appropriate level for tests and full reporting of outcomes |
| <input type="checkbox"/> | <input checked="" type="checkbox"/> | Estimates of effect sizes (e.g. Cohen's d , Pearson's r), indicating how they were calculated |

Our web collection on [statistics for biologists](#) contains articles on many of the points above.

Software and code

Policy information about [availability of computer code](#)

Data collection

Intrinsic and multiphoton imaging were performed using custom software written by Labview 12.0 and 8.5

Data analysis

Data analysis was carried out using Matlab (2016a)

For manuscripts utilizing custom algorithms or software that are central to the research but not yet described in published literature, software must be made available to editors/reviewers. We strongly encourage code deposition in a community repository (e.g. GitHub). See the Nature Research [guidelines for submitting code & software](#) for further information.

Data

Policy information about [availability of data](#)

All manuscripts must include a [data availability statement](#). This statement should provide the following information, where applicable:

- Accession codes, unique identifiers, or web links for publicly available datasets
- A list of figures that have associated raw data
- A description of any restrictions on data availability

All codes are available upon request from the corresponding authors

All data are available at https://github.com/TeamAlbeanu/mosaic_representations

Field-specific reporting

Please select the one below that is the best fit for your research. If you are not sure, read the appropriate sections before making your selection.

- Life sciences Behavioural & social sciences Ecological, evolutionary & environmental sciences

Life sciences study design

All studies must disclose on these points even when the disclosure is negative.

| | |
|-----------------|---|
| Sample size | No sample size calculation was performed. The sample sizes are considered adequate for the experiments and consistent with the literature. |
| Data exclusions | No data was excluded from the analysis. |
| Replication | We have sampled numerous different animals and fields of view and were able to replicate the results across subsets of data. |
| Randomization | Randomization was not relevant to the study. The analysis of the three types of data from glomeruli, mitral and tufted cells was performed first independent of each other and several animals. |
| Blinding | Blinding was not relevant to this study - the analysis of the three types of data from glomeruli, mitral and tufted cells was performed first independent of each other. |

Reporting for specific materials, systems and methods

We require information from authors about some types of materials, experimental systems and methods used in many studies. Here, indicate whether each material, system or method listed is relevant to your study. If you are not sure if a list item applies to your research, read the appropriate section before selecting a response.

Materials & experimental systems

| n/a | Involved in the study |
|-------------------------------------|---|
| <input checked="" type="checkbox"/> | <input type="checkbox"/> Antibodies |
| <input checked="" type="checkbox"/> | <input type="checkbox"/> Eukaryotic cell lines |
| <input checked="" type="checkbox"/> | <input type="checkbox"/> Palaeontology |
| <input type="checkbox"/> | <input checked="" type="checkbox"/> Animals and other organisms |
| <input checked="" type="checkbox"/> | <input type="checkbox"/> Human research participants |
| <input checked="" type="checkbox"/> | <input type="checkbox"/> Clinical data |

Methods

| n/a | Involved in the study |
|-------------------------------------|---|
| <input checked="" type="checkbox"/> | <input type="checkbox"/> ChIP-seq |
| <input checked="" type="checkbox"/> | <input type="checkbox"/> Flow cytometry |
| <input checked="" type="checkbox"/> | <input type="checkbox"/> MRI-based neuroimaging |

Animals and other organisms

Policy information about [studies involving animals](#); [ARRIVE guidelines](#) recommended for reporting animal research

| | |
|-------------------------|---|
| Laboratory animals | Experiments were performed in 12 to 24 weeks old Tbet Cre X Ai38 mice and Tbet Cre X Ai95 mice using multiphoton imaging (males and females) and OMP-Cre X Ai95 mice, OMP-Cre X ReaChR mice and OMP-Cre X ReaChR X Ai95 mice using intrinsic imaging (males and females). |
| Wild animals | No wild animals were used in this study. |
| Field-collected samples | No field-collected samples were used in this study. |
| Ethics oversight | All animal procedures were approved by the Cold Spring Harbor Laboratory Institutional Animal Care and Use Committee. |

Note that full information on the approval of the study protocol must also be provided in the manuscript.